Plasmonic and Magneto-Optical Properties of Nonstoichiometric Indium Nitride Nanostructures

by

Shuoyuan Chen

A thesis

presented to the University of Waterloo

in fulfillment of the

thesis requirement for the degree of

Master of Science

in

Chemistry (Nanotechnology)

Waterloo, Ontario, Canada, 2019

Author's Declaration

I hereby declare that I am the sole author of this thesis. This is a true copy of the thesis, including any required final revisions, as accepted by my examiners. I understand that my thesis may be made electronically available to the public.

Abstract

Localized surface plasmon resonance (LSPR) in semiconductor nanostructures have attracted intense attention recently for its broad application in bio-imaging, chemical sensing, photocatalysis, and photovoltaics. Compared to the LSPR in metallic nanocrystals (NCs), LSPR in semiconductor NCs is highly tunable in the infrared region by tailoring chemical composition and stoichiometry. Moreover, LSPR along with external magnetic field allows the exploration of magneto-plasmonic coupling in single-phase semiconductors, opening up the magneto-optical ways to control charge carriers.

In this thesis, we focus on the LSPR as well as magneto-optical properties of indium nitride (InN), providing valuable insights into the insufficiently researched III-V group semiconductors. Wurtzite phase InN NCs were successfully synthesized using the low-temperature colloidal method, and the plasmon intensity is tunable by changing the synthesis environment and varying doping concentrations of aluminum and titanium ions. Due to the combined effects of conduction band non-parabolicity and intraband transition, our InN NCs with different plasmon intensities have an almost fixed plasmonic energy of 0.37 eV. Besides, the optical bandgap of pure InN NCs ranges from 1.5 to 1.75 eV, depending on the reaction conditions, while that of the Al and Ti-doped InN varies from 1.65 to 1.85 eV. The plasmon-dependent phonon change is evaluated by the Raman spectroscopy. Differences in the longitudinal-optical (LO) phonon mode was observed for InN with high and low plasmon intensity. The magneto-optical properties of InN NCs were measured by the magnetic circular dichroism (MCD). The field-dependence and temperature-independence of the measured MCD spectra were investigated, and the plasmon-induced polarization of carriers was demonstrated. Tuning of the carrier polarization by varying LSPR and

external magnetic field corroborates the hypothesis of non-resonant coupling between plasmons and excitons in a single-phase semiconductor. The results of this work demonstrate that LSPR can act as a degree of freedom in manipulating electrons in technologically-important III-V nanostructures and lead to potential applications in photonics and quantum computing at room temperature. Finally, InN nanowires (NWs) with LSPR were fabricated via low-temperature chemical vapor deposition (CVD) approach, laying the groundwork for the future research of LSPR and magneto-plasmonics in a one-dimensional system.

Acknowledgments

I would like to acknowledge Dr. Carmen Andrei and Nathaniel Smith for their help in TEM and SEM operation, respectively. In addition, I would like to acknowledge Terry for his assistance in MCD spectra collection. My sincere thanks also go to Nazar's group at the University of Waterloo for granting me access to their FTIR spectrometer.

I would like to thank my past and current colleagues, Manu, Vahid, Paul, Natalie, Terry, Hanbing, Susi, Enas, Yunyan, Yufeng, Nathaniel, Walker, and Luna for their support. Special thanks go to Manu and Terry for guiding me through my project and giving me valuable suggestions.

Finally, I would like to express my special thanks to my supervisor, Dr. Pavle Radovanovic, for his continuous support of my study and research. I am much inspired by his patience, enthusiasm, and knowledge. Besides my advisor, I would also like to express my gratitude to the rest of my thesis committee: Dr. Vivek Maheshwari and Dr. Jonathan Baugh for their encouragement and advice.

Table of Contents

List of Figures

List of Tables

List of Abbreviations

a.u.	Arbitrary Unit
ATO	Antimony-doped Tin Oxide
AZO	Aluminum-doped Zinc Oxide
CB	Conduction Band
CBM	Conduction Band Minimum
CD	Circular Dichroism
CVD	Chemical Vapor Deposition
DMF	Dimethylformamide
FTIR	Fourier Transform Infrared Spectroscopy
FWHM	Full Width at Half-Maximum
IR	Infrared
ITO	Tin-doped Indium Oxide
LCP	Left-Circularly-Polarized
LO	Longitudinal-Optical
LSPR	Localized Surface Plasmon Resonance
MBE	Molecular-Beam Epitaxy
MCD	Magnetic Circular Dichroism
MIR	Mid-Infrared
MOCVD	Metal-Organic Chemical Vapor Deposition
MOVPE	Metal-Organic Vapor-Phase Epitaxy
NC	Nanocrystal

NIR	Near-Infrared
NW	Nanowire
ODE	Octadecene
RCP	Right-Circularly-Polarized
SAED	Selected Area Electron Diffraction
SEM	Scanning Electron Microscopy
TCE	Trichloroethylene
TEM	Transmission Electron Microscopy
UV-Vis-NIR	Ultraviolet-Visible-Near-Infrared
VB	Valence Band
VBM	Valence Band Maximum
VLS	Vapor-Liquid-Solid
wz	Wurtzite
XRD	X-ray Diffraction
zb	Zinc-blende

Chapter 1. Introduction

1.1 Intrinsic Semiconductors and Extrinsic Semiconductors

Pure substances can be classified as conductors, semiconductors, and insulators by their electrical conductivity at room temperature. A semiconductor is not completely insulating like an insulator (e.g., quartz), but also not quite conductive as a conductor (e.g., iron). The ability to be conductive is determined by whether there are free carriers in the substance to carry charges around and form currents. In band theory, it means that there exists a partially-filled band, allowing carriers to move freely in that band. For a conductor, i.e., a metal, valence band (VB) and conduction band (CB) are merged together, which means the half-filled top VB is now the CB with free electrons as carriers. For an insulator, the VB is fully filled, and the bandgap is so high that electrons cannot be thermally excited to the CB at room temperature. All the electrons in the insulator are thus localized, and charge flowing is prohibited. In the case of a semiconductor, the bandgap persists, but it is not wide enough to forbid thermal and photonic excitation. Therefore, a limited quantity of electrons is excited to the CB, leaving the equal number of holes in the VB. The electrons and holes are bounded in pairs by the Coulomb interaction and are called excitons. Although some electrons will also relax to the ground state and emit photons during recombination, a certain number of excitons are preserved in the dynamic process to produce carriers in a semiconductor.
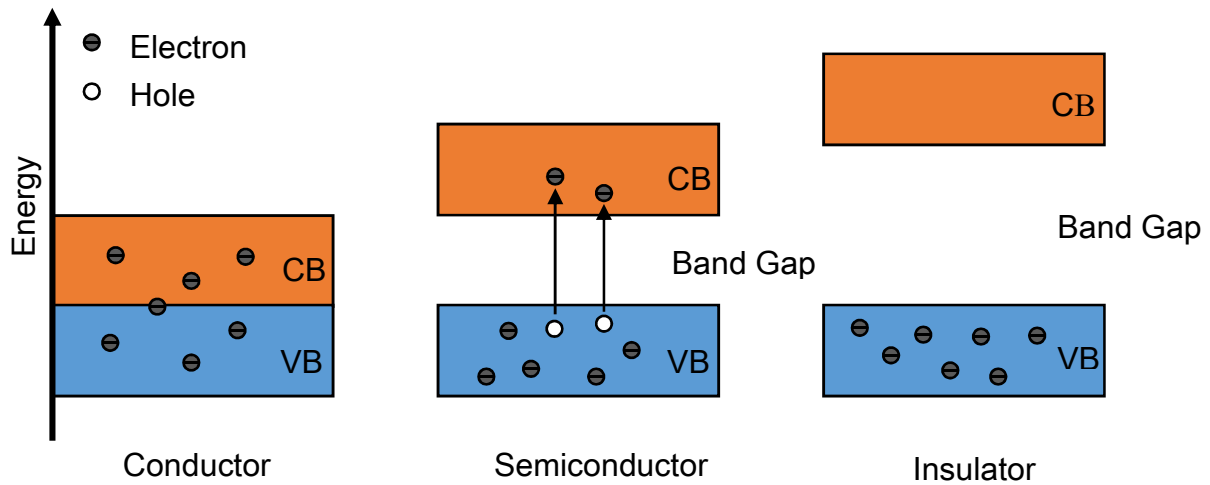
Figure 1.1 Illustration of the band structures of conductor, semiconductor, and insulator.

Exciton behavior depends strongly on the bandgap, which is characterized by not only the energy difference but also the crystal momentum (k-vector) difference between conduction band minimum (CBM) and valance band maximum (VBM). When their k-vectors are the same, the bandgap is considered 'direct', and the excitation and recombination are radiative processes involving excitons and photons solely. When there is a mismatch between the k-vectors of CBM and VBM, the bandgap is 'indirect'. Under this scenario, phonons have to be employed to mediate the momentum difference, which takes extra energy and lowers efficiency.
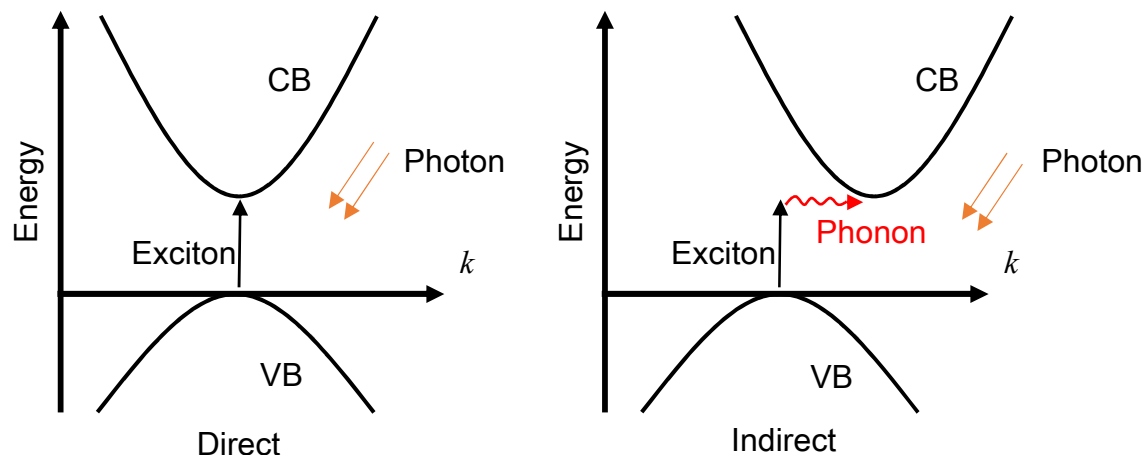
Figure 1.2 Schemes of direct and indirect bandgap.

A pure semiconductor is also called an intrinsic semiconductor, and it has an even value of electron and hole concentration. The carrier density can be improved by adding heterovalent impurity ions into the host lattice and make an extrinsic semiconductor. Treating the band structure alteration in a simplified manner, dopant ions with higher valence can donate excess electrons and therefore promote electron density in the CB. On the other hand, foreign ions with lower valence can trap excited electrons from the VB, leaving an excessive number of holes in the VB. The doped semiconductor is called an n-type semiconductor if electron is the dominant carrier, or a p-type semiconductor if hole is predominant in the charge flowing process.
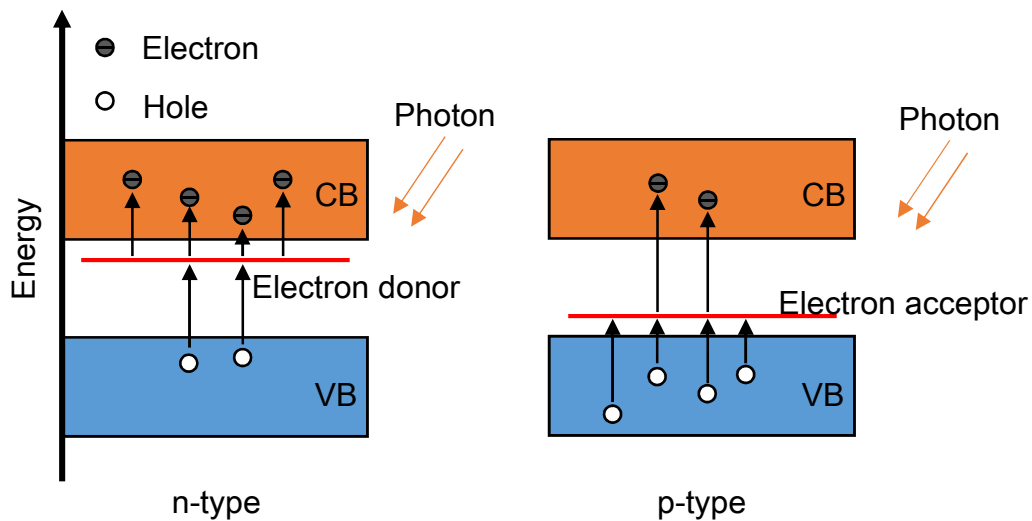
Figure 1.3 Illustration of band structures of n-type and p-type semiconductor.

The ability to control the electrical properties of silicon through doping opened doors for the emergence of the transistor and photovoltaic industry. However, apart from being abundant, cheap, and stable, one big drawback of silicon is its indirect bandgap, causing energy loss in the phonon-assisted transition. It strictly restricts silicon to light-emitting and photovoltaic applications. The relatively large bandgap (1.14 eV) of silicon also limits the ceiling of carrier concentration. Heavy doping has to be applied for high carrier concentration, but energy loss and heat accumulation by electron scattering become non-negligible. Therefore, the investigation of alternative semiconductor materials has become a booming topic in material science.[1]

1.2 Indium Nitride (InN) Nanocrystals (NCs) and Nitrogen Native Defects

III-V semiconductors are potent candidates to replace silicon, which is currently dominating the electronics industry. Compared to II-VI semiconductors, III-V semiconductors have a broader variety of stoichiometry and structures, which offers diverse electronic properties. As a consequence, representative III-V semiconductors, such as In_2S_3 and InSe, are favored in the photovoltaic industry.[1] Indium nitride (InN) is another typical member of the III-V group. It has a narrow direct bandgap of around 0.7 eV and outstanding electron mobility (up to 4000 $cm^2V^{-1}s^{-1}$), making it competitive with silicon in fast-responding electronics and solar cells.[2,3] However, in spite of owning extraordinary electrical properties, single-crystalline InN is expensive and difficult to manufacture. Bulk production of high-quality InN wafer is still unavailable because InN decomposes above 500 ℃, limiting the reaction temperature and thus the quality and yield.[4,5] However, thanks to the compressed alignment and small scale of current electronic devices, InN can yet be integrated into the industry in forms of thin film, nanowire, and nanocrystal.[6–8]

Nanoscale InN has been studied for years, and a common theme is its native nitrogen defects. Due to the requirement of low synthesis temperature, conventional thermal synthesis approaches like metal-organic vapor-phase epitaxy (MOVPE), chemical vapor deposition (CVD), and metal-organic chemical vapor deposition (MOCVD) suffer from low mobility of the deposited atoms, vulnerable to lattice defects.[4,5,9] Native nitrogen defects are ubiquitous, which donate electrons, resulting in n-type conductivity. Fabricated via various methods, InN has a reported carrier density ranging from 5×10^{18} to 5×10^{20} cm^{-3}.[4] The excess electrons trigger Burstein-Moss band-filling effect and push the Fermi level above the CBM. The result is so ingrained that it causes errors in measuring the absolute bandgap of InN, which is still a controversial topic now. An apparent

optical bandgap ranging from 0.9 eV to 1.9 eV has been reported over the years.[3,4,10,11] The generally accepted value for the actual bandgap of InN is 0.65 eV and was measured by infrared luminance.[11]

(a)

(b)
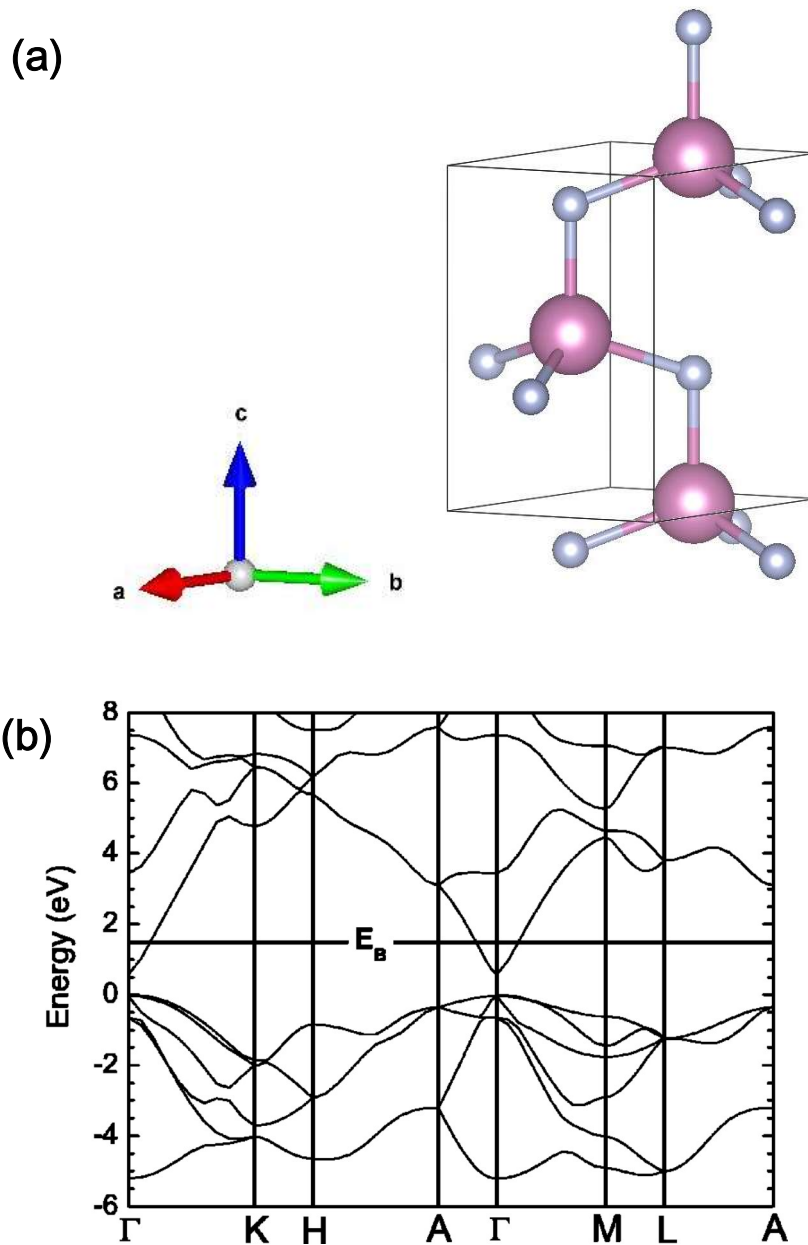
Figure 1.4 The (a) unit cell and (b) electronic structure of *wz*-InN. The unit cell is drawn using the software VESTA. The pink ball represents indium atom, and grey ball stands for nitrogen atom. The electronic structure is calculated using density functional theory within the local density approximation and is obtained from reference 12.

InN predominantly exists in the thermodynamically stable wurtzite phase (*wz*), with indium and nitrogen atoms occupying tetrahedral sites and alternatingly layered in the [001] direction. It has been reported that molecular-beam epitaxy (MBE) growth of InN on an *r*-plane sapphire base can yield a metastable zinc-blende phase (*zb*).[4] Calculations show that the two phases of InN have almost identical direct bandgap (~0.7 eV) and non-parabolic CBMs, except that *wz*-InN has a steeper CBM valley than *zb*-InN, which indicates smaller average effective mass in CBM.[12]

In recent years, liquid-phase syntheses of InN, namely the colloidal and solvothermal methods, utilizing reaction between amide groups and indium salts, have been proposed.[13,14] Many of these researches report high defect concentration along with high carrier density.[13-15] Localized surface plasmon resonance (LSPR) of InN nanostructures is a newly emerged feature which was overlooked before. The first report on the LSPR aspect of InN nanostructures is from Dr. Neale, in which sub-Bohr-radius InN nanoparticles were produced via a colloidal method.[15] However, the plasmon can only be adjusted through adding charge-scavenging agents.[15] The tuning of LSPR of InN through doping is nonetheless fruitless so far.

1.3 Localized Surface Plasmon Resonance (LSPR)

Decades of study in nanotechnology has shown that nanoscale materials have unique properties compared to bulk materials. One of these peculiarities is that metallic nanoparticles have high absorption in the visible and ultraviolet range, which is only confined to surfaces in bulk.[16,17] These optical responses originate from the resonant oscillation of CB electrons caused by incoming electromagnetic wave.[17–19] In bulk materials, such coupling only exists on the surface because incident light can only penetrate limited depth. When it happens in a nanocrystal, free electrons over its whole volume are polarized and collectively oscillate at the same frequency.[16–19] These electrons absorb photon energy at the resonant frequency and are named plasmons, which results in the formation of a strong absorption band centered at the wavelength corresponding to the resonance of the spectrum. This phenomenon is known as localized surface plasmon resonance (LSPR). Despite the difference in absorption, LSPR also polarizes and enhance the nearby electric field. LSPR coupling between particles increase the local electric field and improve light absorbance within the medium, which allows for sub-wavelength imaging applications.[18,20,21]. The high carrier density at the surface makes it promising in photocatalysis field, which helps to accelerate water splitting and wastewater treatment.[22]

Since LSPR is a collective behavior of free carriers, metallic NCs became an obvious target of interest. Noble metals, which possess both chemical-neutrality and visible-range resonant frequency, have been widely applied in bio-imaging.[23] Nevertheless, plasmon frequency in metallic NCs can only be tuned within a narrow range by size control, which sharply limits their usage in nanoscale integration and low-frequency applications.[19,23] Towards expanding the scope

of LSPR, semiconductors, whose carrier concentrations can be manipulated *in situ*, draw researchers' attention.
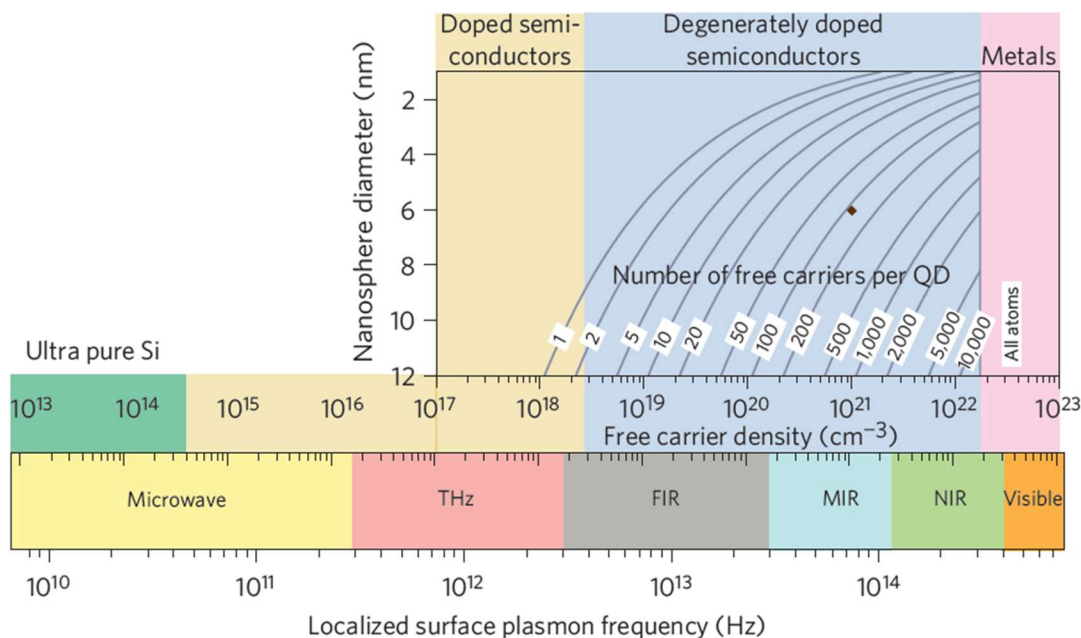
Figure 1.5 LSPR frequency dependence on free carrier concentration in quantum dots (QDs).[24] Quantum dots are spherical NCs.

Though first discovered in metals, LSPR has already been extended to semiconductors in recent years. Semiconductors with sufficiently high carrier density are all potential LSPR candidates.[25] Currently, there are two ways to achieve this goal. The first one is doping semiconductors with another element to introduce extra electrons or holes. This method succeeds in producing many well-known n-type semiconductor NCs such as Sn-doped In_2O_3 (ITO) and Sb-doped SnO_2 (ATO).[26–28] However, it is hard to make p-type plasmonic semiconductors based on this approach. Provided that most semiconductors are of II-VI or III-V groups, it requires group I/VII dopants to form p-type II-VI semiconductors or group I/II/VI/VII dopants to form p-type III-

V semiconductors. These dopants are either too reactive to get incorporated evenly in NCs or too small to substitute host cations.[29] Besides, it is also difficult to overcome the naturally formed native n-type defects in some semiconductors (e.g., CdO, InN), which hinders any possible p-type doping. The second route is to induce cation or anion vacancy in existing semiconductors, which can be applied to produce both n-type (WO_{3-x}) and p-type ($Cu_{2-x}S$) plasmonic semiconductors.[30,31]

Due to the relatively low free carrier density compared to metals, the absorption of LSPR in semiconductors are usually within infrared (IR) span. Its peak absorption can be easily tuned over a broad range of wavelengths through applying an electric field, varying chemical composition, and oxidizing/reducing post-treatment.[32–34] Previously unreachable by metal LSPR, it opens a gate towards photon-matter interaction in IR range and dynamic control of LSPR properties. Besides, studying the differences and similarities between n- and p-type plasmonic semiconductors is an attractive topic.[24] Incorporating LSPR directly into semiconductor devices for optical sensing and spin control starts burgeoning among engineers as well.[24]

LSPR orients in free electrons and thus can be quantitatively understood through solving the Maxwell equation. The effective dielectric constant in the Maxwell equation is demonstrated as function $\varepsilon(\omega)$, which is strictly affected by the frequency of incident light.[19,24] The equations are listed below:

$$\varepsilon(\omega) = \varepsilon_\infty - \frac{\omega_p^2}{\omega^2 + i\omega\Gamma} \qquad\qquad \text{Equation 1}$$

$$\omega_p^2 = \frac{ne^2}{\varepsilon_0 m^*} \qquad\qquad \text{Equation 2}$$

where ε_∞ is the high-frequency dielectric constant, ω_p is the bulk plasma frequency, ω is the frequency of incident light, n is the free carrier concentration, e is the elementary electronic charge, ε_0 is the permittivity of free space, and m^* is the effective mass of the electrons within the crystal.

Here ω_p is controlled by free carrier density n and effective mass m^*. Many metallic NCs have high electron density (10^{22}-10^{23} cm^{-3}), which is the root of their LSPR.[19] m^* is usually a constant in semiconductor, but it can vary as a function of k-vector in semiconductors with nonparabolic CBM. Nonparabolic CBM is a feature often observed in degenerate semiconductors (e.g., CdO, ITO, and AZO) and certain narrow-band semiconductors (e.g., InN).[10,35,36]

The size and morphology of the NCs contribute significantly to LSPR because they determine interior electron scattering, which is indicated as Γ in Equation 1.[17] ε_∞ is closely related to the material itself and is $6.7\varepsilon_0$ for InN, which explains why the resonance conditions of plasmonic NCs are sensitive to solvents and surface ligands. The Drude model can be used to describe the overall LSPR frequency of spherical NC:

$$\omega_{\text{Drude}} = \sqrt{\frac{\omega_p^2}{m_e(\varepsilon_\infty + 2\varepsilon_m)} - \gamma^2} \qquad \text{Equation 3}$$

where m_e is the mass of an electron, ε_m is related to surrounding dielectric environment, γ is the damping parameter of electron scattering that results in the broadening of LSPR peak. The resonant frequency can be readily altered when plasmonic nanoparticles are exposed to an electron or hole scavenging species.[37]

1.4 Plasmon-Exciton Coupling and Spintronics

Plasmons and excitons are two widely observed light-matter interactions in semiconductor nanocavities. When the plasmonic resonant frequency is close to the excitonic frequency, perturbation between wavefunctions of plasmons and excitons may occur and a new hybrid state, plexciton, forms. Energy exchange between excitons and plasmons can be achieved through plexciton, which is primarily utilized in metal-semiconductor heterojunction interface for optoelectronic enhancement.[38] For instance, light-emitting GaN NWs coated with noble metal are reported to have improved recombination rate and thus increased quantum yield of photoluminescence.[39] Besides, the resonant coupling between plasmon and exciton extends the lifetime and diffusion distance of excitons, which promotes the light scavenging ability of the solar cell.[40]

Recent reports also indicate that spin states of the free electrons can be altered through plasmon-exciton coupling. It is recently demonstrated with Au-nanoparticle-decorated $Pt/BiY_2Fe_5O_{12}$ bilayer films that charge spin states can be controlled by externally triggered plasmon resonance.[41] Earlier, a correlation between the strength of the optical Stark effect and plasmon intensity has been observed in Au-CdSe core-shell NCs.[42] These phenomena offer a new angle towards manipulating carrier spin states, which adds new directions in spintronics.

Spintronics is a newly emerged field in electronics that studies the simultaneous control of charge and spin in semiconductors.[43] The new spin degree of freedom can enhance the capacity and speed of current electronic devices. Furthermore, quantum information processing with careful control over spin qubits can significantly shrink device size and improve efficiency. Manipulating spin of electrons using magnetic field is of great research interest under this category.

Though heavily studied in metal/semiconductor nanocomposites, plasmon-exciton coupling inside one single-phase plasmonic semiconductor attracts little attention due to the large energy discrepancy between the two excited states. Our group's previously reported the splitting of the excitonic states upon excitation with circularly polarized light in an external magnetic field, which shows dependency on plasmon energy and type.[44,45] The observations hint the existence of non-resonant plasmon-exciton coupling in semiconductor NCs, which could open up many new applications. Studies on a greater diversity of plasmonic semiconductors are required, and the internal mechanism needs to be explained.

1.5 Magneto-plasmon Coupling and Magnetic Circular Dichroism (MCD)

Apart from the spin angular momentum arrangement, orbital polarization can also be induced by an external magnetic field. Under simultaneously applied electric and magnetic field, free electrons oscillating at the resonant frequency experience Lorentz force, which results in a collective helical or cyclotron motion:

$$\mathbf{F} = -e\mathbf{E} - e\mathbf{v} \times \mathbf{B}$$

<div align="right">Equation 4</div>

where e is the electron charge, $\mathbf{E}$ is the electric field of incoming light, $\mathbf{v}$ is the group velocity of electrons, and $\mathbf{B}$ is the external magnetic field.

The incident light can be divided into left-circularly-polarized (LCP) and right-circularly-polarized (RCP) terms, which are degenerate at zero field and therefore indistinguishable.

However, the two modes split when a magnetic field is exerted along the light propagation direction:

$$\Delta\omega = |\omega_B - \omega_0| = g(\omega_0)\mathbf{B} \qquad \text{Equation 5}$$

$$\omega_B = \omega_0 \pm \frac{\omega_C}{2} \qquad \text{Equation 6}$$

where $g(\omega_0)$ is the proportionality constant and ω_B (ω^+, ω^-) is the separated magneto-plasmonic mode. Therefore, the frequency and absorption of LCP and RCP light deviate, which is also named cyclotron splitting. The above magneto-optical features can be well characterized using magnetic circular dichroism (MCD) spectroscopy, which measures the absorption difference between the LCP and RCP beam.

MCD spectrometer differs from conventional circular dichroism (CD) spectrometer in that it does not require chiral samples for CD signal. It contains a superconducting electromagnet to produce strong magnetic field enough to split energy states into sub-states by their spin and/or orbital angular momentum. The white incident light first passes through a monochromator to modulate the wavelength. It is then divided into two beams and filtered by the right circular polarizer and left circular polarizer separately to generate even amount of LCP and RCP light. The two elliptically polarized beams are then recombined onto the sample, and the resulting ellipticity (θ) is recorded.
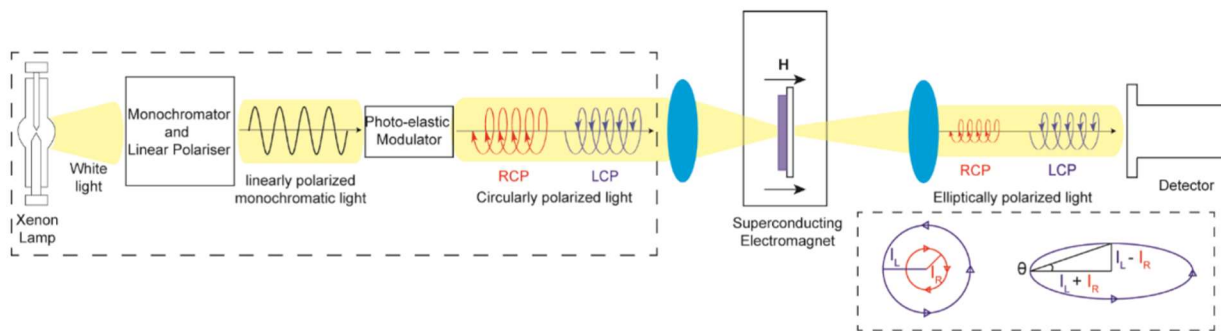
Figure 1.6 Scheme of MCD Spectrometer.[44]

To compare quantitatively, the raw signal needs to be normalized to the same absorbance (A) using Equation 7, and the MCD intensity is described by Equation 8:

$$\frac{\Delta A}{A} = \frac{\theta}{39326 \times A} \qquad\qquad \text{Equation 7}$$

$$\frac{\Delta A}{E} = \gamma \mu_B B \left[A_1 \left(-\frac{\partial f(E)}{\partial E} \right) + \left(B_0 + \frac{C_0}{kT} \right) f(E) \right] \qquad\qquad \text{Equation 8}$$

where A_1, B_0, C_0 are constants related to three unique transitions constituting MCD signal: A, B, C terms, respectively. The three terms are illustrated in Figure 1.7. The A-term corresponds to the transition between VBM and Zeeman-split degenerate CBs, which is only dependent on the magnetic field. The B-term stands for the mixing and perturbation between split bands, which dominates in organic molecules and of little importance in this study. The temperature-and-field-codependent C-term represents the transition from Zeeman-split valence sub-bands to the CBM. The CB splitting resulted from collective helical motion of electrons resembles the A-term Zeeman splitting in MCD. However, split excited-states are influenced by spins, which are properties of

individual electrons, while magneto-plasmon represents collective helical motion of localized electrons.
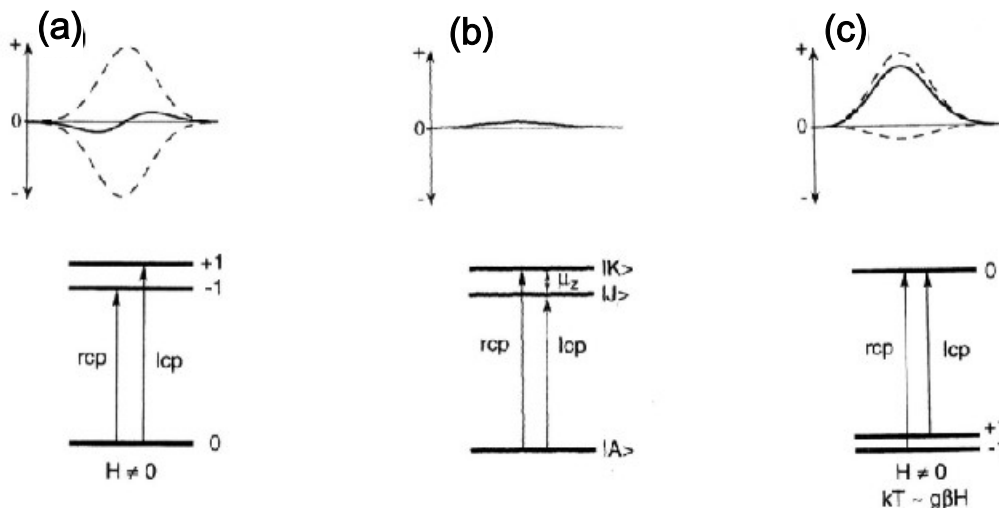
Figure 1.7 Scheme of MCD terms: (a) A-term, (b) B-term, and (c) C-term.[46]

The cyclotron splitting at resonant frequency was first observed in gold nanoparticles.[47] Later, IR MCD spectroscopy gave similar results on various types of doped plasmonic semiconductor NCs, while the splitting does not exist in their non-plasmonic twins.[48] Among these studies, the MCD intensity is found to be linear with the magnetic field. The fact that the intensity is temperature-independent and does not saturate at high field contradicts the prediction made by Curie paramagnetism. It indicates that the linear dependence is derived from the excess charge carriers and can be considered a characteristic of LSPR.

Nonetheless, the same linear dependence of MCD signal on the field is probed at the excitonic frequency of plasmonic semiconductors. The MCD intensity is also temperature-independent and correlates with plasmon intensity. Our group's recent publications point out that such similarity

may indicate that there exists an intrinsic exciton-plasmon coupling as a general phenomenon in single-phase plasmonic semiconductor NCs.[44,45,49] It is hypothesized that such non-resonant coupling via vast energy difference is enabled by phonon oscillation, but so far more evidence is needed to elucidate the mechanism of this phenomenon.

1.6 InN Nanowire (NW) Growth

Geometry plays an essential role in the plasmonic properties of InN. Up to now, InN nanospheres, nanodisks, nanorods, and nanowires (NWs) have been synthesized.[5,50,51] Even with the same In/N ratio, variance in shape still influences not only the intensity but also energy of the plasmonic absorption.[31,51] Among these shapes, anisotropic ones receive special attention because the non-uniform charge distribution gives rise to additional plasmon modes. For example, two "in-plane and out-of-plane dipoles" in nanodisks result in two LSPR modes which can be clearly identified in the absorption spectra.[52,53] Similar optical responses are expected for nanorods in analog with metal nanodisks and nanorods.[54] In an extreme case like NW, one sharp peak in IR range may be observed due to the diminution of out-of-plane LSPR modes, like in the case of $Cu_{2-x}S$ NW.[55] Furthermore, the opportunity to manipulate magnetic field responses via shape or magneto-crystalline anisotropy in III-V NWs can be particularly attractive.[56,57]

A nanowire may exhibit quantum confinement in the radial direction and therefore possess distinct electronic properties.[58] Unlike nanoparticles, which cannot be directly integrated into circuit design, the combination of NW and LSPR enables a powerful platform for device building.[59] Some works have demonstrated using plasmon modes on NWs as waveguides and even

as the subwavelength laser source.[21,60,61] Other works have shown spin-field-effect transistor devices based on semiconductor NWs.[62]

Plasmonic NWs, just like NCs, need to have a diameter smaller than the resonant wavelength to generate localized plasmon modes, which means electron oscillation is distributed over the whole volume without dephasing.[63] Since plasmonic InN NCs has a resonant wavelength in IR region, it is possible for InN NWs to maintain LSPR properties even at the diameter of 100 - 200 nm.[55] This diameter also falls into the regime where CVD method is suitable, which is one of the most significant components of this project.

There are already pioneering papers related to the synthesis of InN NWs using CVD method, but the goal of high-yield and high crystallinity has not been accomplished yet.[7,64–66] The most studied and optimized way by far is a gold-catalyzed process based on the vapor-liquid-solid (VLS) mechanism.[67–69] One big challenge is from the low decomposition rate of the gaseous nitrogen precursors, i.e., NH_3 and N_2H_4, resulting in low deposition efficiency. Though increasing temperature can solve the problem, the low decomposition temperature (420 ℃~600 ℃) of InN presents high incompatibility.[9]

VLS was first proposed in the 1940s.[70] It innovatively uses gravity to promote epitaxial growth. The method was initially designed to rapidly grow single-crystal Si whiskers on Si wafer with Au catalyst and was later applied to the synthesis of semiconductor NWs.[68] VLS approach can be fulfilled through CVD, MBE, or laser ablation.[71,72] Among them, CVD has been widely chosen as the platform for high yield, crystallinity, and for economic considerations.[69]

Here we introduce the VLS method to synthesize InN in our work. Excessive indium powder is used as a reactant, and the whole reaction is carried out under NH_3 flow. As is illustrated in Fig. 1.8, gold droplet is utilized as a catalyst, which is formed by annealing gold thin film. Indium and NH_3 react at the surface of the gold to produce InN. Meanwhile, with a continuous supply of NH_3 and indium vapor, the concentration of InN in the gold droplet reaches supersaturation. InN is forced to precipitate beneath the droplet and form a nanowire, during which process nitrogen defect takes place. The diameter of the NW is mostly determined by the size of the droplet, which makes it tunable.
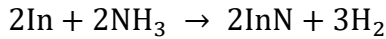
$$2In + 2NH_3 \rightarrow 2InN + 3H_2 \hspace{3cm} \text{Equation 9}$$
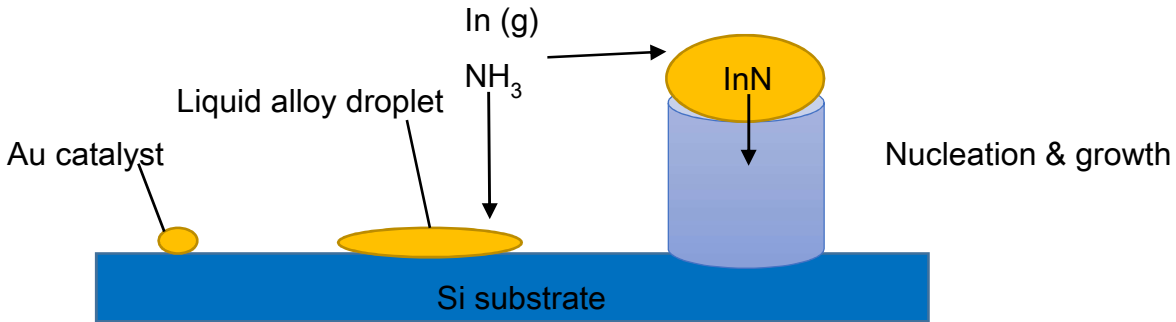
Figure 1.8 Scheme of VLS mechanism for InN fabrication.

A frequently encountered issue in VLS growth of InN NWs is that products are always accompanied by a large number of unwanted structures such as nanocrystals and nanosheets.[7] The phenomenon happens because the growth rate in all directions are similar and the gravitational direction is not predominately favored. The factors CVD system offers to impact NW growth are temperature, pressure, and flow rate. Since InN NW syntheses in CVD occur in a very narrow low-

temperature region (500-700 ℃) and already require high pressure to prevent decomposition, tuning them proves to be hard. So far, control over morphology is challenging. It is predictable that configuring that with our CVD equipment is going to be a challenging task.

1.7 Motivation and Scope of this Thesis

The motivation of this thesis is to manipulate LSPR properties in semiconductor nanostructures via multiple approaches and explore the multi-functionality LSPR could bring to the light-matter and spintronic applications. The exciton-plasmon and magneto-plasmonic coupling in the semiconductor is becoming an emerging new field that could yield future breakthroughs in quantum information technologies. Manipulation of carrier polarization using circularly-polarized light grants new ways to encode information in charges at room temperature. Furthermore, instead of carefully engineering metal/semiconductor conjunctions to achieve the same goal, the homogeneity and intrinsic tunability of semiconductor plasmon by stoichiometry control and doping lowers the manufacturing difficulty and allows easy incorporation into our current semiconductor-based electronics industry.

As the exciton-plasmon coupling hypothesis has not developed into a mature and applicable theory, one big task is to study the magneto-optical properties of a diverse base of plasmonic semiconductors and expand the universality of the hypothesis. The LSPR in II-VI semiconductors has been well studied during the last decade and, as an alternative, I wish to experiment on III-V semiconductors to extend our understanding on semiconductor LSPR. Furthermore, it is anticipated that the polarization of carriers in III-V semiconductor NCs can be achieved using circularly-polarized light and a magnetic field.

For the above reasons, this thesis focuses on the InN NCs and NWs. The fundamental goal is to tune the plasmon in colloidal InN by changing synthesis conditions and by doping. The colloidal InN system also offers an excellent opportunity to combine both quantum confinement and CBM nonparabolicity to tailor LSPR behavior. How these changes of plasmon affect the magneto-plasmon-induced exciton splitting of InN NCs is another big focus of this thesis. With the help of MCD, exciton splitting of III-V plasmonic semiconductor is reported for the first time. By comparing the MCD spectra, new information is revealed about the non-resonant nature of plasmon-exciton interaction in semiconductor NCs and the generality of exciton-plasmon coupling could be corroborated.

Finally, thin plasmonic InN NWs are grown to lift current LSPR study from zero-dimension to one-dimension. NW is a great platform to study the effect of anisotropy on carrier behaviors. In the future, magneto-optical properties of current can be explored, and the possible spin-current-generation that arises from the exciton-plasmon coupling can be analyzed.

In the above studies, multiple characterization tools are employed to study the optical, crystalline, and magnetic properties of InN nanostructures. LSPR tunability is demonstrated, and results are discussed. Apart from the universal application of semiconductor LSPR like IR sensing and bio-imaging, the magneto-plasmonic coupling and polarization of carriers observed opens up the possibility of a future platform for quantum technology.

Chapter 2. Experimental Methods

2.1 Materials

All chemicals except octadecene were used as received without any further purification. Indium powder (99.99%), indium sulfide (In_2S_3, 99.99%), anhydrous aluminum fluoride (AlF_3, 99%) and anhydrous manganese chloride ($MnCl_2$, 99.99%) were purchased from Strem Chemicals. Sodium amide ($NaNH_2$, 98%), HNO_3 (70%), oleylamine (70%), trimethyloxonium tetrafluoroborate (Me_3OBF_4, 95%), octadecene (ODE, 90%), trichloroethylene (TCE, 99.5%) and n,n-dimethylformamide (DMF, 99.8%) were purchased from Sigma-Aldrich. High purity (grade 5) ammonia and argon were purchased from Praxair Inc. ODE was heated overnight at 110 °C under vacuum and stored in the glovebox before use.

2.2 Synthesis Methods

2.2.1 Synthesis of Pure InN Nanoparticles

The synthetic method for indium nitride (InN) NCs in this research is based on the procedures reported by Rémi Beaulac.[8] In an Ar-filled glovebox, 0.163 g (0.5 mmol) In_2S_3, 0.195 g (5 mmol) $NaNH_2$, and 10 mL ODE are mixed in a 50 mL three-neck round-bottom flask. The flask is then sealed with rubber septa and clamped to maintain the internal pressure. The mixture is vigorously stirred and heated to 250 ℃ in one hour under various gaseous conditions (constant Ar flow,

constant NH_3 flow, sealed with Ar inside, sealed with NH_3 inside). It is then maintained at 250 ℃ for a certain amount of time (2h, 3h, 4h, 5h) before cooling down to room temperature.

The post-synthesis processing starts with centrifuging for the raw product. It is then sonicated with toluene for 5 min to clear ODE residue away. Afterward, the product is centrifuged out and washed with ethanol. It is later on sonicated with 3.5% HNO_3 for 10 min to remove indium metal side-product. After centrifuging and ethanol-washing, the resultant particles are capped with oleylamine ligands through a 30-min sonication in oleylamine. After centrifuging, residual In_2S_3 precursors can be separated from the suspension. The solution is washed with ethanol and dispersed in toluene, which is later centrifuged again to wash out any insoluble impurity. The InN nanoparticles in toluene are subsequently precipitated out and re-dispersed in TCE for optical measurement.

A portion of the sample in TCE is taken out for the ligand exchange process. The InN NCs are washed out with ethanol and re-dispersed into hexane. The ligand-stripping agent, Me_3OBF_4, is dissolved in a polar solvent, DMF. The immiscible hexane and DMF solution are mixed in a 1:1 ratio under vigorous stirring for half an hour. It can then be observed that all particles are dispersed in DMF and leave a colorless hexane phase, which indicates the successful detachment of oleylamine. The process aims at removing organic molecules so a good TEM result can be obtained.

2.2.2 Synthesis of Aluminum Doped InN Nanoparticles

The Al-doped InN NCs ias synthesized in a similar manner as InN. NCs with a few modifications. Variable amount (mol) of $AlCl_3$ is added during preparation while the same amount (mol) of indium precursors are deducted to keep the total amount of cation congruent for all samples. The flask is then purged with high-purity Ar and sealed up. The reaction container is held at 250 ℃ for 2 h before cooling down naturally to room temperature. The post-synthetic treatment is the same as that of pure InN NCs.

2.2.3 Synthesis of Titanium Doped InN Nanoparticles

All procedures remain the same as Al-doped InN except that the dopant precursor is replaced with anhydrous $TiCl_4$.

2.2.4 Synthesis of InN NWs

The InN NWs are synthesized using a three-zone CVD furnace. The synthesis method is inspired by a paper by L.C. Chen *et al.*, which is mentioned in the introduction.[68] Indium powder are placed in one ceramic boat, and a piece of 2-nm-gold-coated Si or SiO_2 wafer is carefully laid face-down on top of the indium source, which is then placed in the center of the furnace. The quartz tube was purged under 200 sccm Ar flow for one hour and then heated to 480 ℃. It then maintains the temperature under 30 sccm-NH_3-flow protection for 10 hours. The whole experiment is conducted under atmospheric pressure.
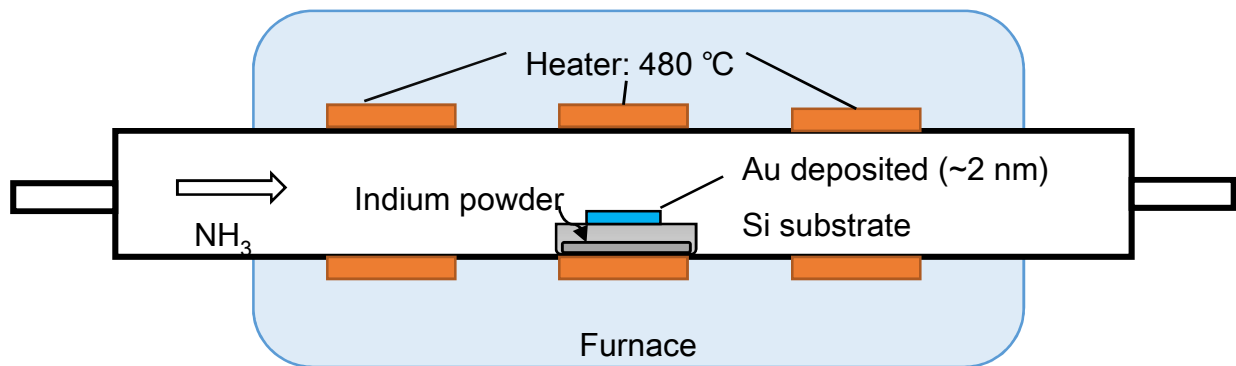
Figure 2.1 Scheme of CVD experimental set-up.

2.3 Characterization Techniques

2.3.1 Powder X-ray Diffraction (XRD)

XRD is an essential tool to determine the crystallinity of the obtained nanoparticles and NWs. The measurement was performed on an INEL X-ray diffractometer. The analyzed sample is placed on a rotating aluminum sample holder and illuminated with a beam of monochromatic Cu Kα1 X-ray (λ=1.5406 Å). Constructive interference of the incident and reflected X-rays due to scattering in periodic crystal lattices can unveil the crystal structures of the samples. The phase of InN can be characterized by comparing with reference XRD patterns. Furthermore, an estimation of the nanocrystal size can be obtained by the Scherrer equation,

$$L_{hkl}=k\lambda/(\theta) \hspace{4cm} \text{Equation 10}$$

where L_{hkl} is the mean diameter of the targeted sub-micrometer particle, k is shape factor, λ is X-ray wavelength of the instrument, B is the full width at half-maximum (FWHM) of one diffraction peak, and θ is the Bragg angle of that peak.

2.3.2 Ultraviolet-Visible-Near-Infrared (UV-Vis-NIR) Spectroscopy

UV-Vis-NIR Spectroscopy refers to recording sample absorption spectra in the UV-Vis-NIR region. The instrument used for such purpose in our lab is Varian Cary 5000 spectrophotometer. It has an extended measurement range from 175 nm to 3300 nm, which is able to cover both the bandgap and the onset of plasmonic absorption peaks of InN samples. In this experiment, well-dispersed InN nanoparticles were measured directly in TCE suspension. Due to strong solvent absorption in the NIR section (>2500 nm), selected samples were deposited on clean quartz substrates and then measured to achieve the full potential of the machine. Therefore, the simultaneous comparison of LSPR peak and band edge on between samples is made possible.

2.3.3 Fourier Transform Infrared (FTIR) Spectroscopy

In order to cover the feature of InN LSPR in the mid-IR region, Fourier-transform infrared (FTIR) spectroscopy was performed on Bruker Tensor 37 FTIR spectrometer. The instrument is able to collect sample absorption data from 500 to 4000 cm^{-1} with a resolution of 0.5 cm^{-1}. In this measurement, InN suspension was drop-casted onto a KBr pellet before use. Consequently, useful information on the organic groups attached to InN surfaces also presented on the spectrum.

2.3.4 Raman Spectroscopy

Raman spectroscopy detects vibrational phonon modes on InN nanoparticles, which reveals structural information. A helium-neon laser (λ=633 nm) serves as the light source in our measurements. InN nanoparticles were dried into powder first and placed on a silicon substrate during measurement.

2.3.5 Scanning Electron Microscopy (SEM)

SEM gives topographic images on the scale of tens of nanometers, providing information on yield, length and overall morphology of as-synthesized NWs. A rough determination of elemental ratio in the NW can be obtained through the Energy Dispersive X-ray spectroscopy (EDX) in the same instrument. Field emission SEM measurements were done on a LEO 1530 with an operating voltage ranging from 5 kV to 20 kV.

2.3.6 Transmission Electron Microscopy (TEM)

TEM provides full morphological information on a nanometer scale, and its EDX can give higher precision on the atomic ratios of different elements than a SEM. Moreover, selected area electron diffraction (SAED) can be used to determine the lattice structures of the samples. An ultra-thin sample needs to be specially prepared for the high-energy electron beam to tunnel through. The transmitted electrons convey knowledge on interior construction. High-resolution TEM is utilized to get high-quality images on selected nanoparticles and nanowires to study grain boundaries, defects, and secondary phases. In this work, measurements were performed on a JEOL

2010F microscope operating at 200 kV. The InN nanoparticles were dispersed in DMF and NWs are dispersed in ethanol. They were then deposited on 400 mesh TEM copper grids before use.

2.3.7 Magnetic Circular Dichroism (MCD) Spectroscopy

MCD measurements were executed on a Jasco J-815 spectropolarimeter. It is capable of generating a variable magnetic field (0-7 T) as well as tunable temperature (5-300 K) on the samples. The MCD spectra were collected with respect to absorption spectra from 350 to 800 nm. In this work, samples were drop-casted on strain-free quartz slices to obtain temperature-dependent and magnetic-field-dependent MCD spectra. The spectra with the valid fitting method can yield photo-magneto properties of ion species and defects.

Chapter 3. Study of LSPR in InN NCs

Pure InN NCs with different plasmon intensity is produced by adjusting reaction time and synthesis environment. Equation 11 shows that a large amount of NH_3 gas is generated during the process. By either sealing or venting the flask, the amount of NH_3 inside can be controlled. The partial pressure of NH_3 in the four conditions are arranged in increasing order in Table 3.1.

$$In_2S_3 + 6\,NaNH_2 \rightarrow 2\,InN + 3\,Na_2S + 4\,NH_3 \qquad\qquad \text{Equation 11}$$
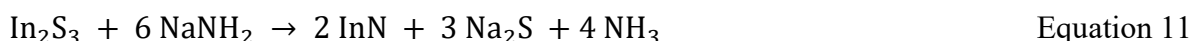
	Estimated Amount of Gas (mol)	Estimated Partial Pressure of NH_3 (atm) at 250 ℃
constant Ar flow (conAr)	2.2×10^{-3} Ar	0
constant NH_3 flow (conNH₃)	2.2×10^{-3} NH_3	1
sealed with Ar inside (sealAr)	2.2×10^{-3} Ar $+ 3.2\times10^{-3}$ NH_3	1.4
sealed with NH_3 inside (sealNH₃)	5.4×10^{-3} NH_3	2.4

Table 3.1 Estimated amount of gas and partial pressure of NH_3 under four reaction environments. The volume of gas in the flask before the reaction is estimated to be the same as the volume of the flask (50 mL) and the mole amount is calculated assuming normal temperature and pressure (20 ℃, 1 atm). The amount of NH_3 produced during the synthesis is estimated assuming complete reaction

of Equation 11. The estimated partial pressure is calculated assuming normal temperature and pressure.

3.1 Crystal Structures and Morphology of Pure InN NCs

3.1.1 XRD Pattern of Pure InN NCs
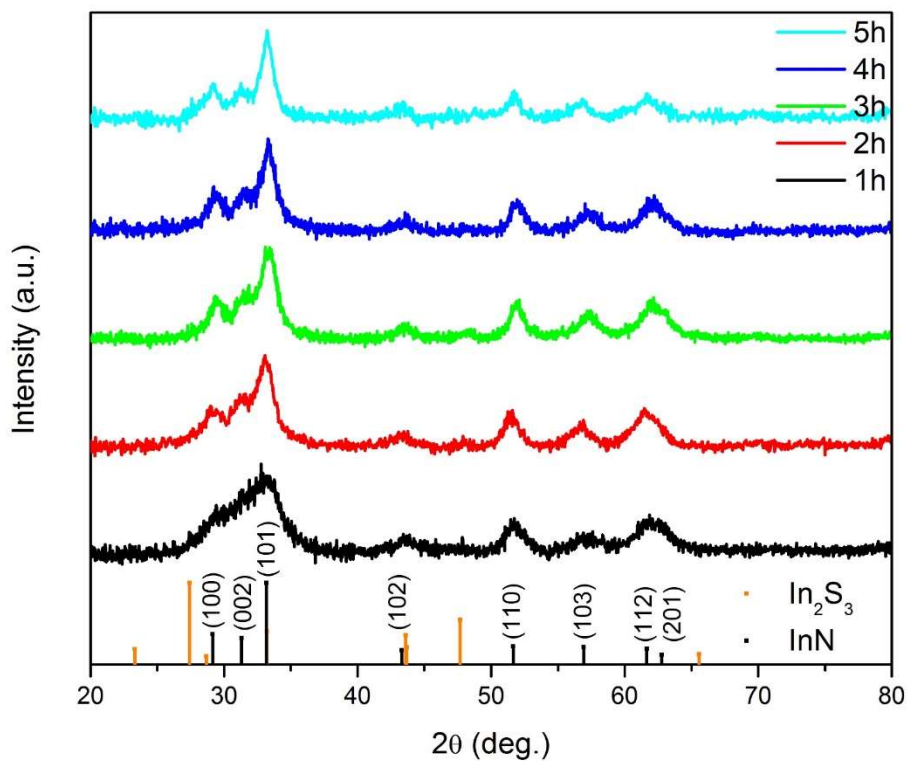
Figure 3.1 XRD of sealAr InN NCs synthesized for different durations. Reference diffraction angles for bulk wz-InN (00-079-3498) and In_2S_3 (01-084-1385) are given as black bars and yellow

bars, respectively with the corresponding planes. The corresponding planes of *wz*-InN are labeled above each reference bar.[73]

Name	Estimated Size (nm)
sealAr-1 h	4.6±0.9
sealAr-2 h	5.2±0.5
sealAr-3 h	5.9±0.7
sealAr-4 h	6.3±0.5
sealAr-5 h	7.7±1.0

Table 3.2 Estimated particle sizes of samples in Figure 3.1, calculated according to the Scherrer equation.

Figure 3.1 illustrates the XRD patterns of sealAr InN NCs synthesized for different durations (1–5 h), which is identified using powder XRD. It is evident that all patterns agree with the reference *wz*-InN, indicating good crystallinity and no secondary phases. Except for the sealAr-1h sample, all patterns have clearly identifiable peaks. The peak broadening is due to the size effect, as described by the Scherrer equation. The lines are de-convoluted first, and the estimated particle sizes of NCs are then obtained and listed in Table 3.2. As the reaction time lengthens, a small increase in NC size is noted. The results consent to early studies.[8,15]
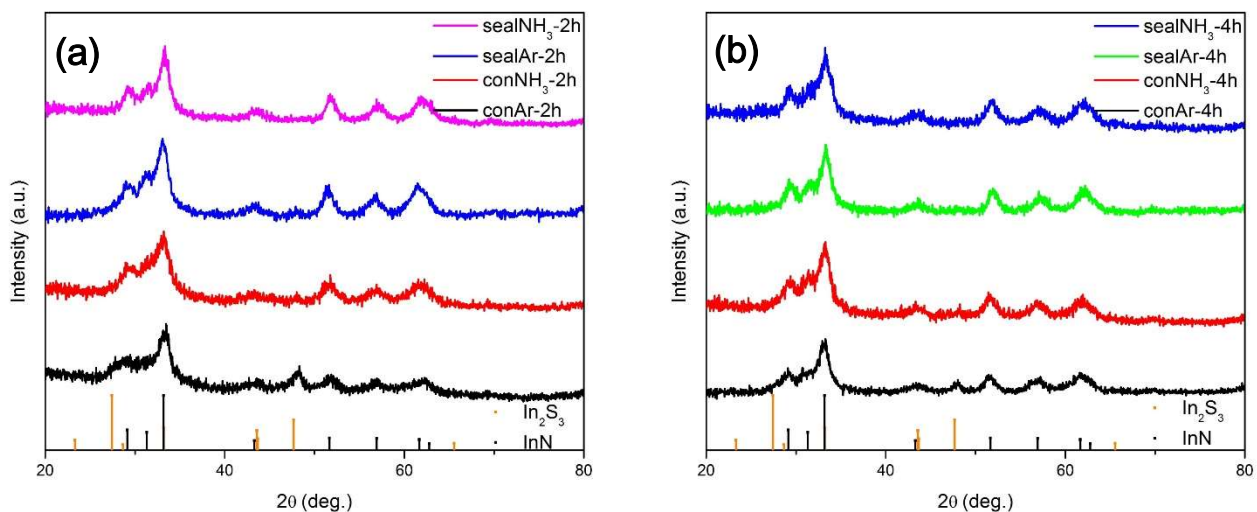
Figure 3.2 XRD of InN NCs synthesized at different conditions but with the same duration. (a) InN NCs synthesized for 2 h and (b) 4 h. Reference diffraction angles for bulk wz-InN (00-079-3498) and In_2S_3 (01-084-1385) are given as black bars and yellow bars, respectively.

	2 h (nm)	4 h (nm)
sealNH$_3$	5.5±0.7	6.3±0.8
sealAr	5.2±0.5	6.3±0.5
conNH$_3$	4.8±0.3	5.9±0.5
conAr	5.2±0.3	5.9±0.9

Table 3.2 Estimated particle sizes of samples in Figure 3.2, calculated according to the Scherrer equation.

From Figure 3.2, we learn that varying gaseous conditions give rise to In_2S_3 secondary phases. By reducing the partial pressure of NH_3, In_2S_3 impurity peak at 48.5^0 gradually emerges. It may be because NH_3 would suppress the recrystallization of In_2S_3 and enhance the reaction yield. The reduction in NH_3 lowers the amount of InN in the resultant solution, which adds to the difficulty in removal of In_2S_3 impurity. The centrifuging procedure to remove In_2S_3 is based on the suspensibility difference between In_2S_3 and InN, which is naturally incapable of removing In_2S_3 completely. It works well only when the yield of InN is high, which makes the residual In_2S_3 plays an insignificant role in characterizations. In addition, it can be concluded from Table 3.2 that the particle size has little dependence on the reaction environment, and reaction time is playing a pivotal role.

3.1.2 TEM Studies of Pure InN NCs
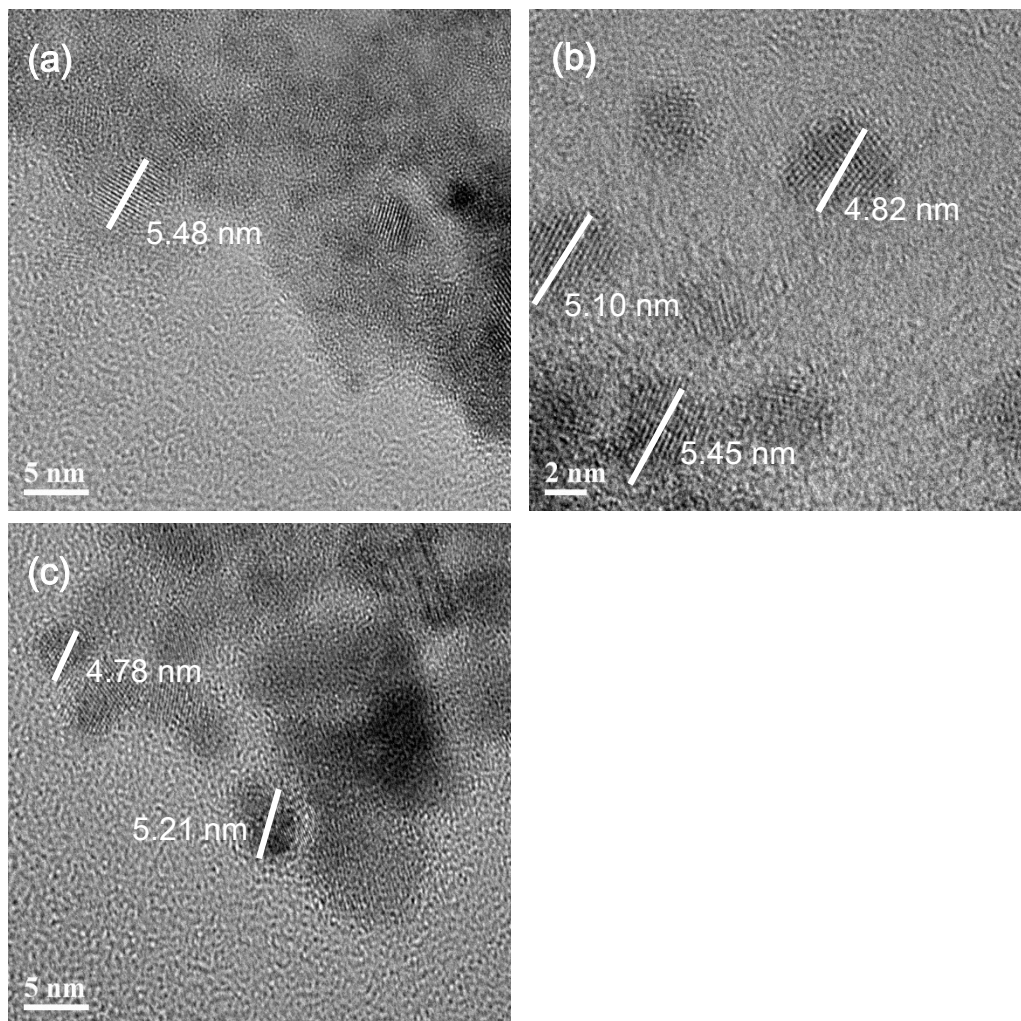
Figure 3.3 High-resolution TEM images of (a) conAr, (b) sealAr and (c) sealNH$_3$ InN NCs synthesized in 4 h. Diameters of representative nanoparticles are labeled.

The TEM images in Figure 3.3 visibly show that the NCs are separated and crystalline. Due to the fact that InN NCs are small and wrapped in oleylamine ligands, certain degrees of aggregation is expected. Since discrete NCs are hard to identify, the sizes of NCs are only estimated by measuring a few chosen NCs labeled in Figure 3.3. The sizes obtained using TEM is

generally 1 nm lower than those obtained with the XRD, but still, the particle sizes are little influenced by the reaction environment.

3.2 Spectroscopic Studies of InN NCs

3.2.1 Absorption of Pure InN NCs

Figure 3.4 illustrates the overall absorption spectra of all pure InN NCs. It is immediately apparent that tuning the LSPR of InN NCs by merely changing the chemical environment is successfully achieved. By increasing the amount of NH_3 involved in the reaction, plasmon intensity increases, and the band edge absorption blue-shifts. Secondly, InN plasmon frequency does not shift much with the intensity change, which agrees with previous reports.[8] InN has a nonparabolic CBM, and the Fermi level lies in the linear range of the band, causing the effective mass to be dependent on the wavevector k. Since the carrier concentration n can also be simplified into a linear function of k, the plasmon frequency, which is majorly determined by n/m^*, ends up being nearly a constant (3000 cm^{-1}).[8] In our case, the constant plasmon wavelength is measured to be around 3300 nm (3030 cm^{-1}). Since the energy is fixed for different LSPR strength, the Drude model is no longer applicable. The literature on determining the carrier density using redox titration and electrochemical cell exists, while attempts on determining the carrier concentration solely from the absorption are not yielding.[8,74] The carrier concentration obtained by another group using the same synthesis method as ours is on the order of 10^{20} cm^{-3}.[8] Thirdly, there is a general tendency of plasmon intensity drop in all reaction conditions when the reaction time increases. It

could be that elongated growing time enlarges the particle size and removes lattice defects, creating better stoichiometry than short growing time.
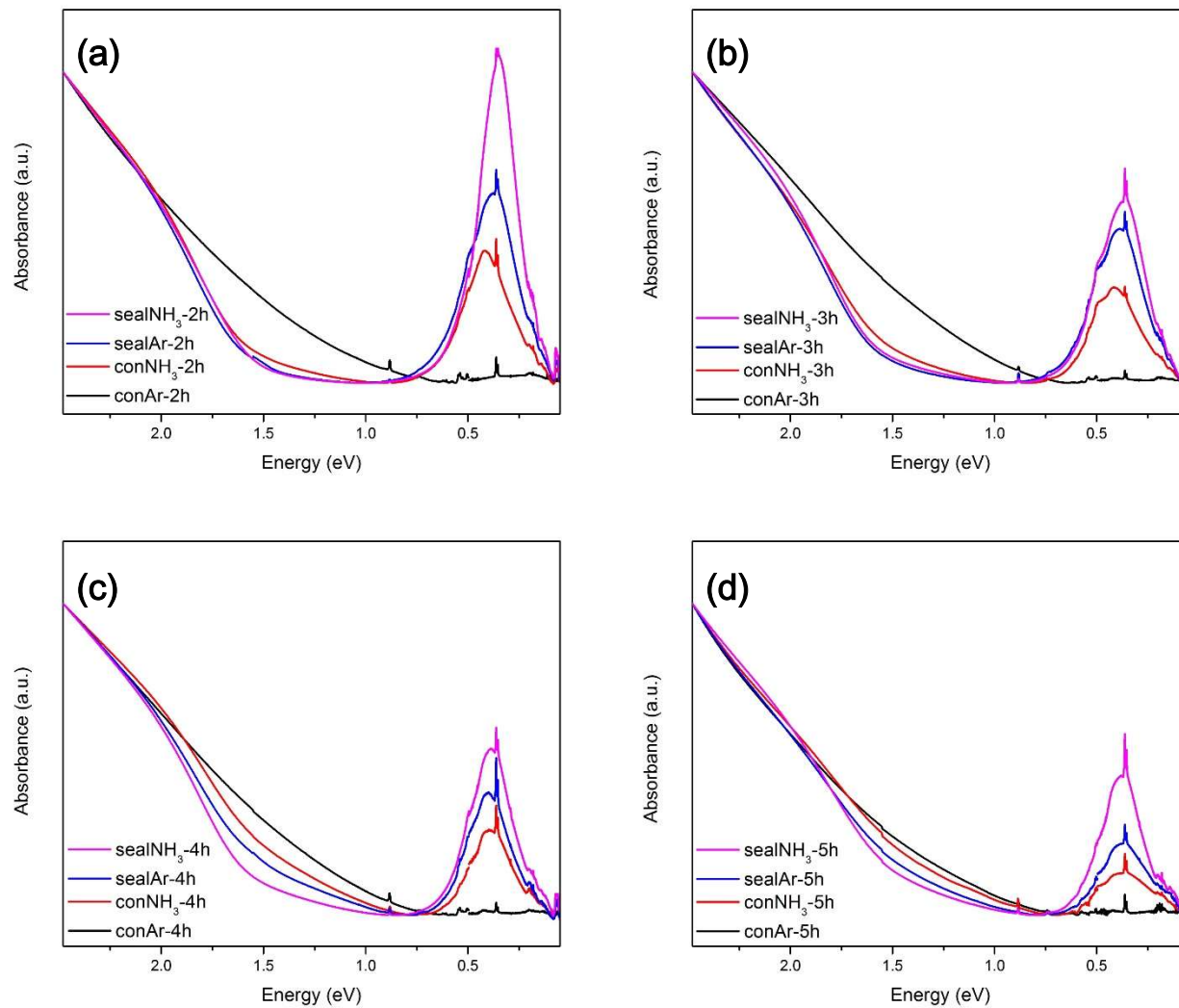
Figure 3.4 Joined absorption spectra of InN NCs synthesized for (a) 2 h, (b) 3 h, (c) 4 h and (d) 5 h. The spectra are obtained from merging UV-Vis-NIR spectra and FTIR spectra.

Figure 3.5 (a) is a typical Tauc plot obtained from Figure 3.4 (c), used to estimate the optical bandgap of InN NCs. Due to the high carrier density caused by the native defects, there are
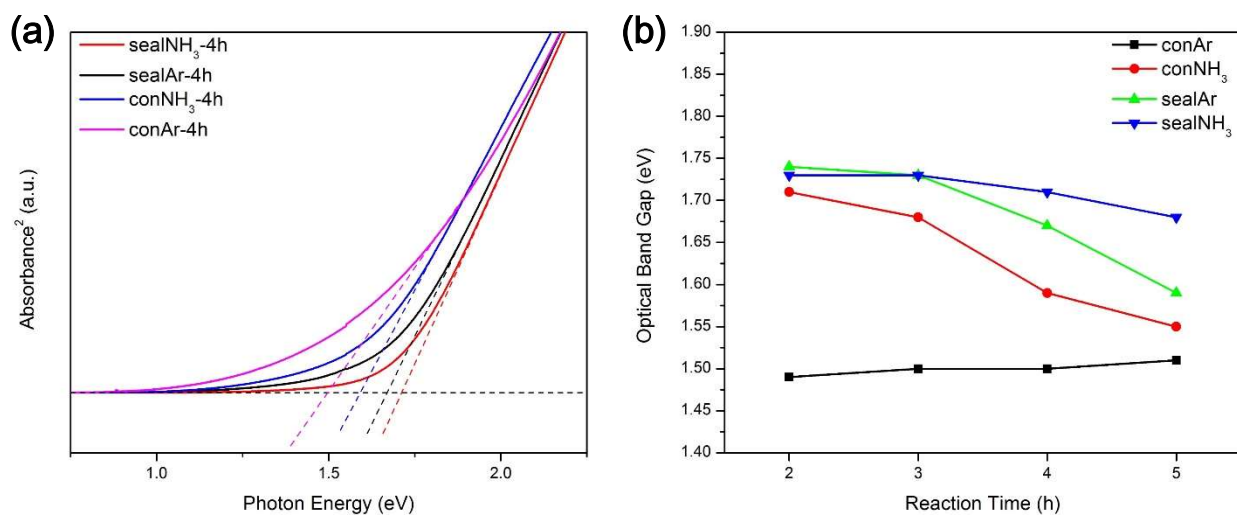
electrons accumulating in the CB, which results in the Burstein-Moss shift. The shift causes the optical bandgap to be larger than the absolute bandgap. The optical bandgaps of all pure InN NCs are comprised in Figure 3.5 (b). In principle, the optical bandgap ought to decrease gradually with the drop of plasmon intensity, which is demonstrated as for the 4 h and 5 h series. However, as the reaction time goes as short as 2 and 3 h, the gradient of the optical band gap becomes significantly smaller. It indicates the existence of bandgap narrowing effect caused by high defect concentration, which compensates the Burstein-Moss effect. Such band shrinkage is often observed in other degenerate semiconductors (e.g., ITO, Sn-doped ZnO) and is also proposed in InN.[75–77] The effect is evident at high carrier density, which equals to high plasmon intensity, effectively creating a ceiling for measured apparent bandgaps at about 1.74 eV. The lowest bandgap measured is 1.5 eV for InN NCs without LSPR, which is still much larger than the reported bandgap of bulk InN (0.65 eV).[11]

Figure 3.5 (a) Tauc plot of sealAr InN NCs synthesized for 4 h; (b) Optical bandgap of InN NCs estimated from the Tauc plots of all InN samples.

3.2.2 FTIR Studies of Pure InN NCs

Figure 3.6 shows the maximum of the intensity-normalized FTIR spectra. It is noticeable that the plasmon peak position remains mostly unchanged. Appreciable blue-shifts are also noted in 2 h and 3 h sample series as plasmon intensity increases. The origin of the shift could be CBM shape change, which is related to the lattice strain. It has been reported that a higher concentration of defects and smaller size would lead to more considerable strain and steeper CBM, where the average effective mass is more significant than that of low concentration.[77] A similar shift of LSPR was reported in InN NCs prepared by pulsed plasma process where the nitrogen-vacancy level was directly tuned.[78] Fixed LSPR frequency was observed in the redox and electrochemical studies of colloidal InN NCs because only the carrier concentration is modified while the defect concentration remains the same.[8,74] The intensity-normalized FTIR spectra of InN synthesized for different durations under the same condition can be found in the Appendix (Figure A1). The plasmon peaks of InN manufactured for varied time lie in a similarly narrow range (500 cm^{-1}) for different reaction atmospheres. It indicates that the impact of reaction time alone is limited.

Here our hypothesis is formulated as follows. Since our experiment methods are inspired by reference 8, the basic resonant frequency for all reaction conditions can be treated as a fixed value (3000 cm^{-1}) first, where only carrier concentration variance is considered. However, the four variant synthesis environments change the nature of InN NCs, modifying the defect concentration as well. Therefore, the additional change of CBM and effective mass m^* is taken into consideration. If the carrier concentration n remains the same, the bulk plasma frequency ($\sim n/m^*$) will increase with reducing defect concentration, leading to the blue-shift of LSPR frequency. Meanwhile, in our experiment, the defect concentration is also the driving force of carrier

concentration. Therefore, high defect concentration corresponds to high plasmon intensity. Reduction in plasmon intensity indicates blue-shift of plasmon frequency. The shift is more pronounced in NCs produced with shorter duration (e.g., 2 h) because the lattice strain is more substantial and defect concentration is generally higher than in long synthesis time (e.g., 5 h) under all reaction conditions.
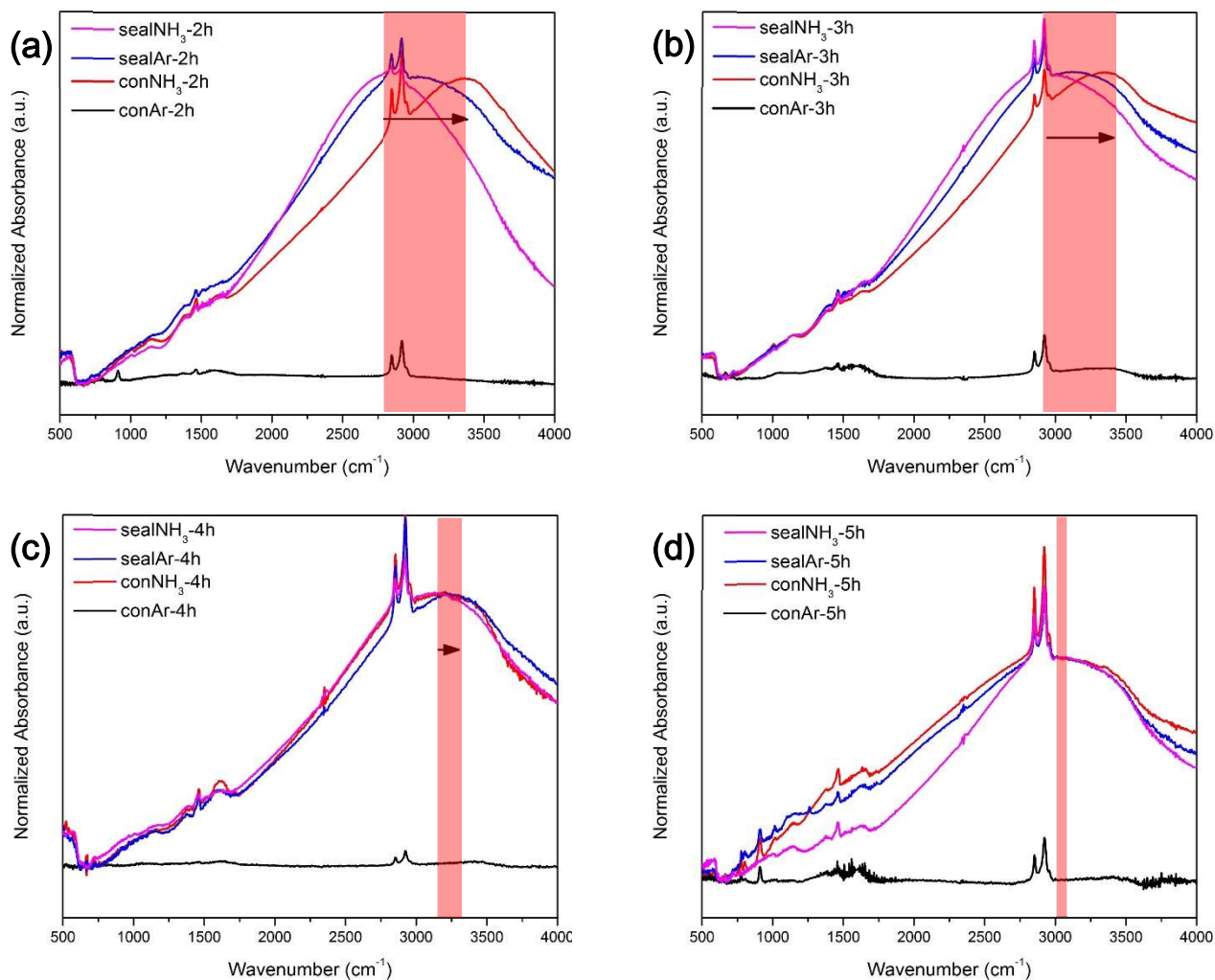
Figure 3.6 Normalized LSPR absorption spectra of InN NCs in the IR range. The graphs are arranged by the reaction time: (a) 2 h, (b) 3 h, (c) 4 h, and (d) 5 h.

To conclude, it is hypothesized that the shift of plasmon energy is controlled by the combined effect of defect density and carrier density. Change in carrier concentration does not impact plasmon frequency, while reduction in defect concentration (decreasing plasmon intensity) causes plasmon frequency to blue-shift. A detailed calculation is beyond the scope of this thesis.

3.2.3 Raman Spectra of Pure InN NCs

Figure 3.7 is a comparison of Raman spectra between sealAr InN (strong plasmon) and conAr InN (no plasmon). The peaks at 458 cm^{-1} and 613 cm^{-1} correspond to the E_2 (high) and A_1 (LO) modes, respectively.[79] The E_2 (high) and A_1 (LO) for bulk InN are at 488 cm^{-1}, 586 cm^{-1}, so our result shows that the two modes are much closer to each other in NCs, which agrees with the finding that the energy gap between two modes shrinks as the size decreases.[51] It can also be seen that the ratio of E_2 and A_1 is higher in conAr samples than sealAr, indicating potential effects of plasmons on phonons. Moreover, a new peak emerges at 588 cm^{-1} in sealAr-2h, which in some studies, is called M_2 mode and is observed only when strong electron accumulation happens.[77] Some studies attribute M_2 mode to crystal imperfections while others consider it to be a plasmon-phonon coupled-mode split from LO.[76,84] Since sealAr-2h does have a very high plasmon intensity and thus has a very high carrier density, there is a high possibility of plasmon-phonon coupling in InN NCs.

The plasmon-phonon coupling could be the missing piece of explaining the non-resonant exciton-plasmon coupling in semiconductors. The polar A_1 mode, which is a longitudinal-optical (LO) phonon mode, is often referred to as exciton-plasmon coupled-mode because its energy and strength depend on both the excitation frequency and carrier concentration. [76,79,79] In this work, the correspondent changes in LSPR and A_1 mode indicate that A_1 mode is relevant in exciton-plasmon coupling. However, whether the mentioned changes are really purely controlled by carrier concentration lacks discussing. The lattice strain, or the nitrogen defect concentration, could be the real driving force, meaning that the correlation between plasmon and the polarized phonon

mode is mediated by defect-related scattering. Therefore, more insights could be obtained by performing Raman spectroscopy on redox processed InN NCs.

Phonon plays a pivotal role in the hypothesis of exciton-phonon coupling mentioned in section 1.5.[43,44] It is expected to transfer angular momentum from cyclotrons to excitons through magneto-plasmonic modes. It has been reported that both excitons and plasmons couple with phonons and energy exchange is attainable.[76,79] Therefore, an analogous chirality exchange between excitons and plasmons through A_1-mode phonons could be possible too, since they are all polar quasiparticles and similar transfers have already been observed in 2-dimensional semiconductors.[81,82]
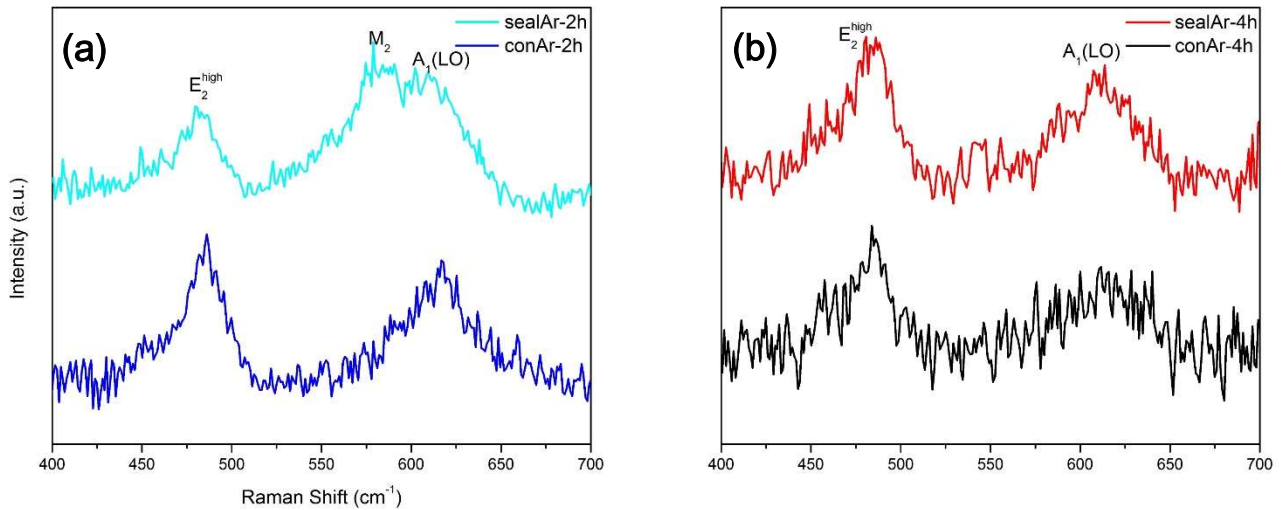
Figure 3.7 Raman spectra of InN NCs with different plasmon intensity. (a) Raman spectra of sealAr and conAr InN synthesized for 2 h; (b) Raman spectra of sealAr and conAr InN synthesized for 2 h.

In summary, colloidal InN NCs with tunable LSPR are synthesized with success by changing the chemical atmosphere for the first time. The as-synthesized InN NCs are small particles (4-7 nm) with quantum confinement and have good crystallinity. The correlated changes of band-edge and plasmon-peak absorption were demonstrated. Moreover, Raman studies on InN reveal potential plasmon-phonon coupling, bridging the gap between excitons and plasmons.

Chapter 4. Study of LSPR in Doped InN NCs

4.1 Crystal Structures and Morphology of Doped InN NCs

4.1.1 XRD Pattern of Doped InN NCs
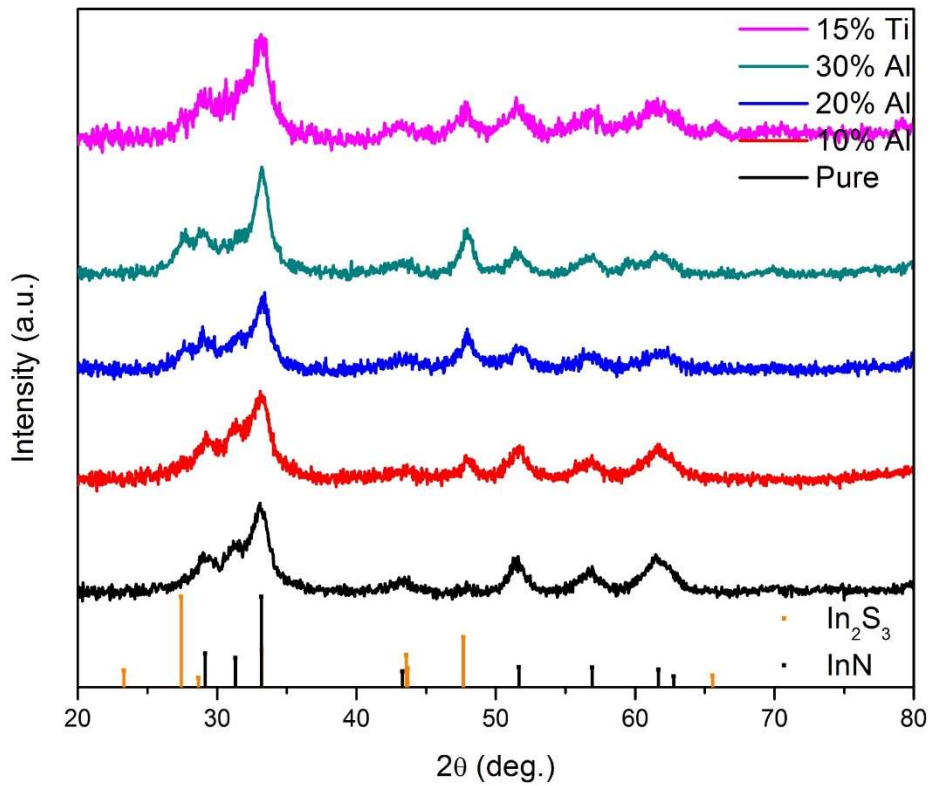
Figure 4.1 XRD patterns of InN NCs synthesized with different starting ratio of dopants (Al and Ti).The bars at the bottom are reference lines of In_2S_3 and wz-InN, respectively.

Name	Estimated Size (nm)
15% Ti	4.9±0.4
30% Al	5.0±1.2
20% Al	5.1±1.1
10% Al	5.2±0.4
Pure	5.2±0.5

Table 4.1 Estimated particle sizes of samples in Figure 4.1, calculated according to the Scherrer equation.

The XRD patterns shown in Figure 4.1 are all mainly composed of InN. Regardless of dopant types, as the ratio of the dopant precursors increases, the impurity phase (In_2S_3) consequently increases. It is possibly because the high doping ratio leads to low yield of InN NCs, which makes the centrifuging method to separate them from impurity rather difficult, as has been discussed in Section 3.1.

Table 4.1 comprises the estimated particle sizes of doped InN NCs with the help of the Scherrer equation. It is clear that doping does not change the size of the InN NCs and all NCs have the size of around 5.1 nm.

4.1.2 Elemental and TEM Studies of Doped InN NCs

Name	Starting Dopant(Al/Ti)/In Ratio	Final Dopant/In Ratio
10% Al-doped InN	0.11	0.07 ± 0.01
20% Al-doped InN	0.25	0.11 ± 0.02
30% Al-doped InN	0.43	0.18 ± 0.04
40% Al-doped InN	0.66	0.26 ± 0.03
5% Ti-doped InN	0.05	0.02 ± 0.01
10% Ti-doped InN	0.11	0.02 ± 0.02
15% Ti-doped InN	0.18	0.05 ± 0.01
20% Ti-doped InN	0.25	0.07 ± 0.03

Table 3.2 The atomic ratio of dopant (Al/Ti) over Indium in doped InN NCs obtained using EDX. The second column lists the starting ratio of chosen dopant. The final concentration of indium is obtained by subtracting In_2S_3 concentration from the total indium concentration, where In_2S_3 concentration is deducted from Sulfur concentration.

Table 4.2 lists the real dopant concentration inside the resultant InN NCs. Though the dopant/In ratio is generally lower than the starting ratio of the corresponding precursor, it is still evident that increasing stating ratio will effectively result in the rise of the final ratio. Besides, the doping efficiency of Al ions is higher than that of Ti ions.
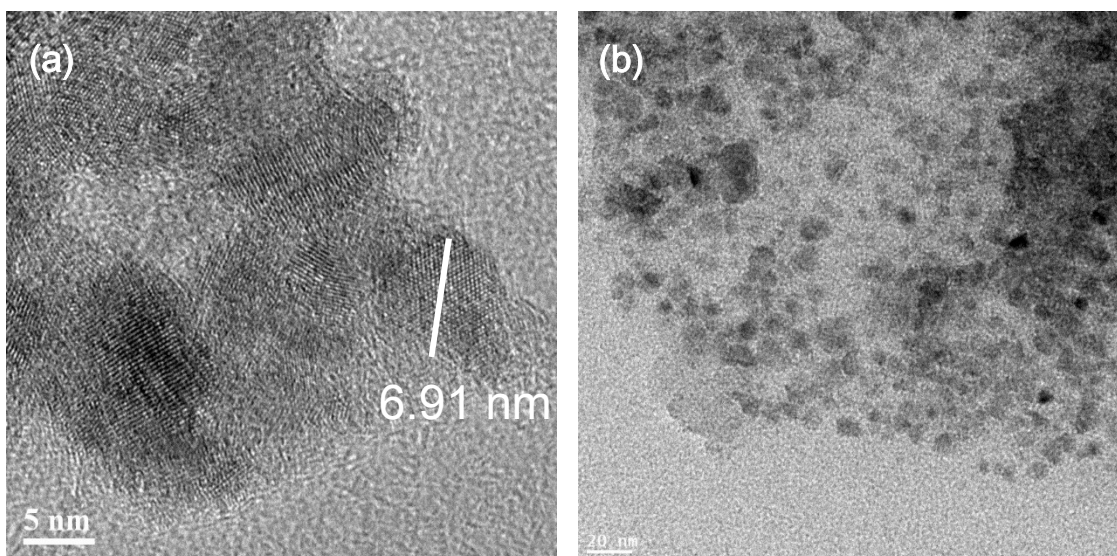
Figure 4.2 (a) High-resolution TEM image of 30%Al-doped InN NCs; (b) Overview of 30%Al-doped InN NCs.

Figure 4.2 (a) shows the high-resolution TEM image of 30% Al-doped InN NCs, which suggests clear crystallinity of as-synthesized NCs. The average size of the NCs is 6.35 nm, which is about 1 nm larger than the estimated size from the XRD results. The particles in Figure 4.2 (b) are distinguishable, but the aggregation is evident. The size distribution diagram (Figure. A2) can be found in the Appendix.

4.2 Spectroscopic Studies of Doped InN NCs

4.2.1 Absorption of Doped InN NCs
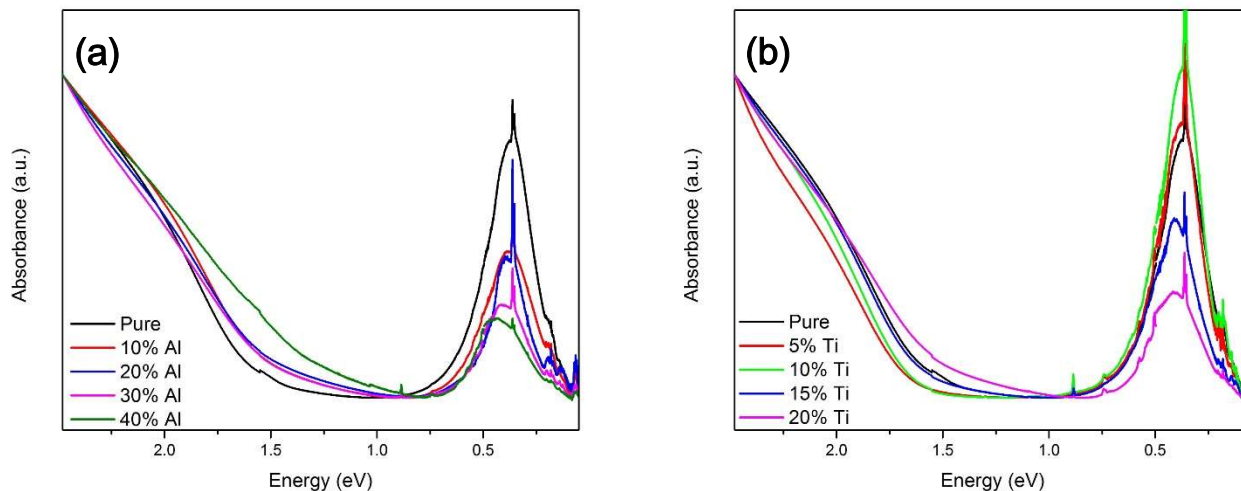
Figure 4.3 Joined absorption spectra of InN NCs synthesized with different starting ratio of (a) Al and (b) Ti precursors. The spectra are obtained from merging UV-Vis-NIR spectra and FTIR spectra.

Figure 3.4 illustrates the overall absorption spectra of Al- and Ti-doped InN NCs. It can be observed that the LSPR absorption declines with the growing incorporation of Al dopants. The plasmon rises with the addition of Ti ions and peaks at 10% Ti-doped InN. Continuing increasing Ti precursors beyond 10% gradually quenches LSPR. The XRD studies from the last sub-section indicate the presence of In_2S_3 impurities. Since In_2S_3 has a larger bandgap (2.2 eV) than InN and has never been reported to have plasmonic absorptions, they will not affect the determination of bandgap and LSPR of InN NCs.[83]
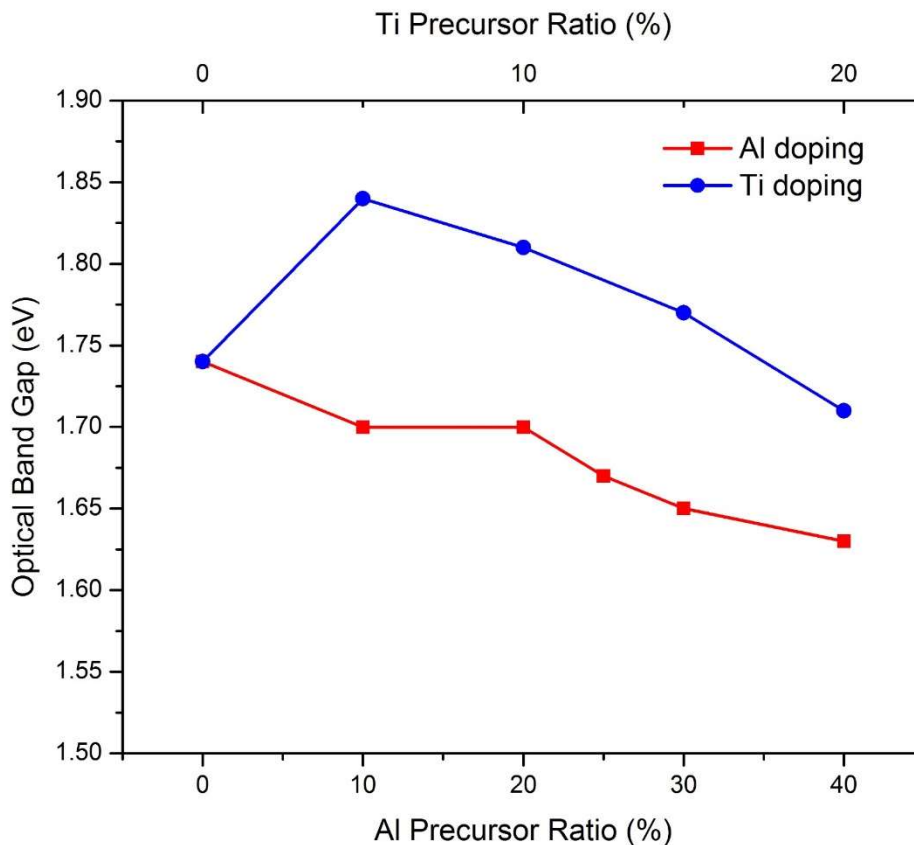
Figure 4.4 Optical bandgap of InN NCs estimated from the Tauc plots of doped InN samples. The red squares represent the optical bandgaps of InN NCs with varying Al starting ratio; the blue circles represent the optical band gaps of InN NCs with different Ti starting ratio.

As is demonstrated in Figure 4.4, the range of optical bandgap caused by external dopants is about 0.2 eV (1.63 – 1.84 eV), which is not significant at all. Such resilience is in good agreement with 2 h pure InN NCs, where all three plasmonic samples share a similar value (1.74 eV) of optical bandgap regardless of intensities. Moreover, a correspondence between plasmon intensity and apparent bandgap is also observed. Regardless of dopant types, sample with low plasmon absorption intensity has small optical bandgap.
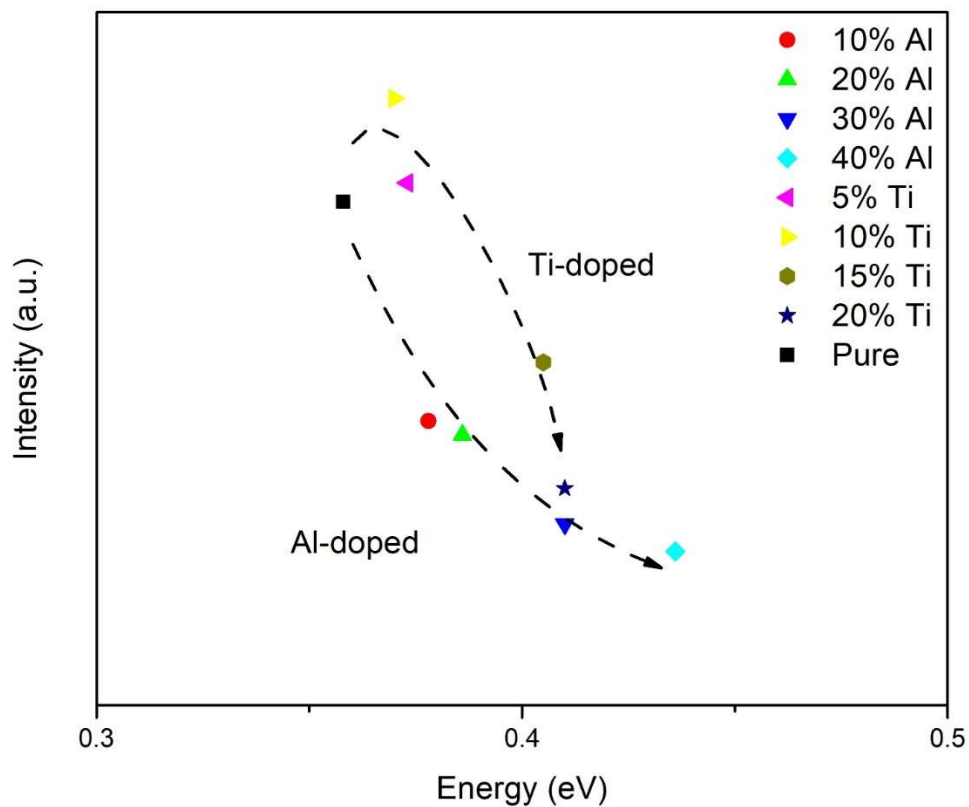
Figure 4.5 The intensity and energy of plasmon absorption maxima of InN NCs with different Ti and Al starting ratio.

Figure 4.5 concludes the LSPR absorption peak intensities and their corresponding energy. It confirms that the energy of LSPR in colloidal InN NCs is confined in a very narrow range (0.4 ±0.05 eV). However, it is also noticeable that there is a relation between plasmon intensity and its energy. Similar to pure InN NCs, the plasmon absorption blue-shifts as its maximum intensity drops.

4.2.2 FTIR Studies of Doped InN NCs
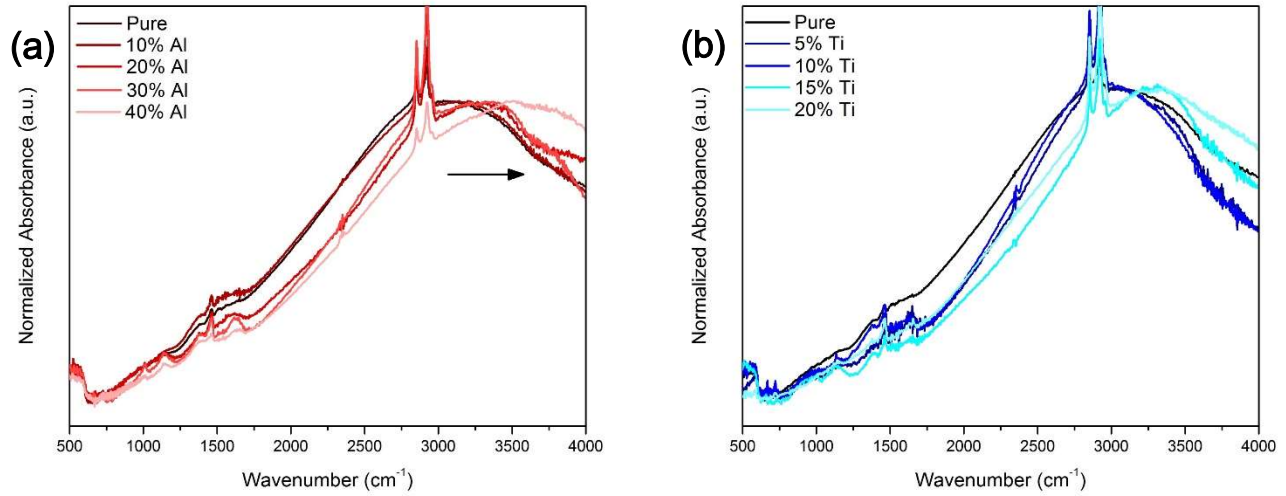
Figure 4.6 Normalized LSPR absorption spectra of (a) Al-doped InN NCs and (b) Ti-doped InN NCs in the range from NIR to MIR in the unit of wavenumber.

Figure 4.6 shows that the LSPR maxima of both Al and Ti-doped InN NCs are confined in a narrow range (3000 – 3600 cm^{-1}), reasonably consistent with those of pure InN NCs synthesized in 2 h. It is also noted that the plasmon frequency blue-shifts as its intensity decreases, regardless of dopant types. This phenomenon is apparent in Al-doped InN NCs, where LSPR absorption blue shifts and drops in intensity as the Al starting ratio increases. For Ti-doped InN NCs, plasmon peak absorption of 5% and 10% Ti-doped samples stay at 3000 cm^{-1}, whose plasmon intensities are higher than pure InN, while the LSPR maxima of 15% and 20% Ti-doped samples red-shifts with the decline of plasmon intensity. Since the energy shift is observed in both pure and doped InN, a direct correlation between plasmon intensity and frequency can be formulated. Our results suggest that InN NCs with high resonant frequencies (high energy) have relatively low intensity.

4.2.3 Raman Spectra of doped InN NCs
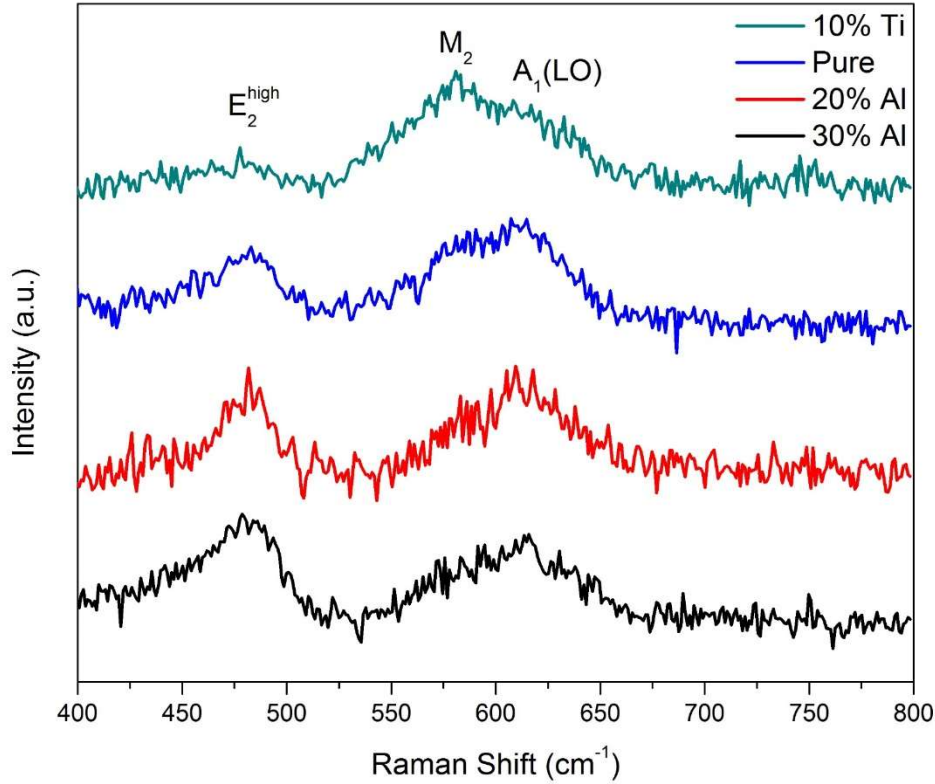
Figure 4.7 Raman spectra of InN NCs with different starting dopant ratio. The plot is so arranged that the plasmon intensity of measured samples decreases from top to bottom.

As is illustrated in Figure 4.7, the spectra are ranked in the decreasing order of plasmon intensity. The positions of the peaks corresponding to E_2 (high) and A_1 (LO) transitions are consistent across all samples and are not affected by the impurity ions. A decrease in the ratio of E_2 (high) over A_1 (LO) is notable, along with the increase in the plasmon intensity. Moreover, it is clear that as the plasmon intensity goes up, the intensity of the M_2 mode at 588 cm^{-1} gradually

increases. By adding different impurities to the host lattice, carrier concentration, and defect concentration change at the same time. It makes it hard to determine whether electron concentration or lattice strain is the driving force of the change in the Raman spectra. All in all, it can be induced from our Raman results that the plasmon intensity rather than the dopant species has the ability to impact phonon modes.

In this chapter, we demonstrate the control of LSPR of colloidal InN NCs through isovalent and aliovalent doping for the first time. Systemic tuning in plasmon intensity is achieved with different starting ratio of Al and Ti. The frequencies of the LSPR absorption of the doped InN NCs distribute closely around 3000 cm^{-1}. Combined with the IR results of pure InN NCs, it can be proposed that plasmon intensity is reversely dependent on the frequency. Our Raman results suggest that LSPR has a strong influence on the polar A_1, M_2 phonon mode. Such influence can be gradually tuned by varying dopant concentration and is unrelated to the dopant species.

Chapter 5. Magnetoplasmonic Studies of InN NCs

To study the magneto-optical properties of InN NCs with different plasmonic strength as well as extending our understanding of plasmon-induced carrier polarization in the III-V group semiconductors, MCD spectroscopy was carried out upon the 4-hour series of InN NCs with varying plasmonic intensities.

Figure 5.1(a) and (b) show the band-edge absorption along with the variable-field MCD spectra of sealNH$_3$-4h collected at 300 K. For the first time in III-V group plasmonic materials, a strong one-side MCD signal is observed, indicating the polarization of excitons. The splitting of the excitonic states depends on whether angular momentum transfers from magnetoplasmonic cyclotron modes to the CB excited states, which is material-specific. Though reported in ITO NCs as well, the details of the internal mechanism of such polarization are still lacking.[48] The signals of InN NCs are weak because the bandgap absorbance of the drop-casted InN films is low. However, a linear dependence of MCD intensity over the applied magnetic field is still very notable in Figure 5.1 (c), which has been reported in II-VI group plasmonic system as well.[44,45] Figure 5.1 (d) demonstrate the stability of MCD signal at different temperatures, proving that it is almost entirely made up of MCD A-term and have little contribution from Curie paramagnetism.
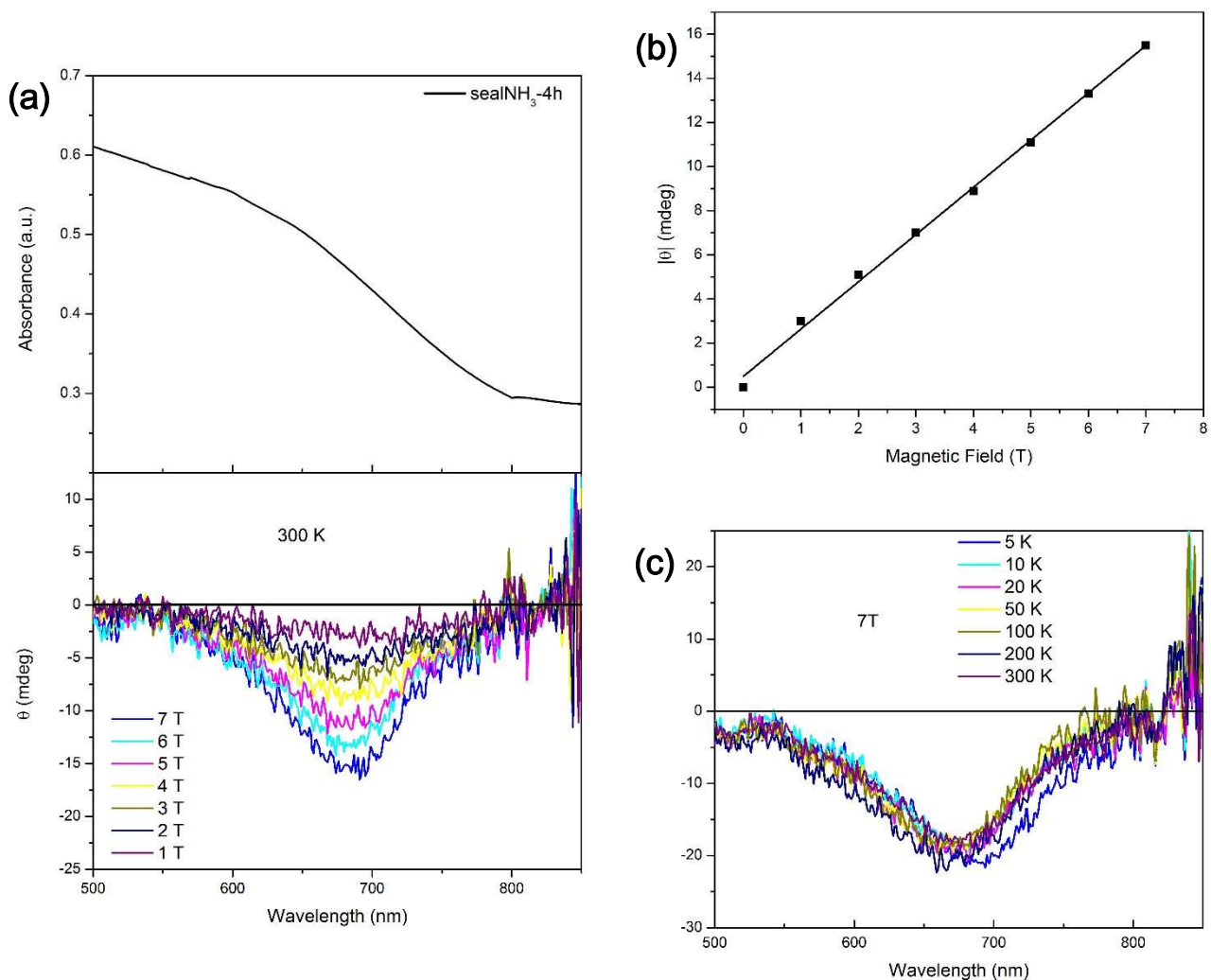
Figure 5.1 (a) Absorption and MCD spectra of sealNH$_3$-4h InN NCs collected at 300 K with various magnetic fields applied. (b) Magnetic field dependence of MCD peak intensity recorded at 685 nm for InN NCs in (a); the black line is the linear fit to the black data points. (c) The 7 T MCD spectra of InN NCs collected at various temperatures.
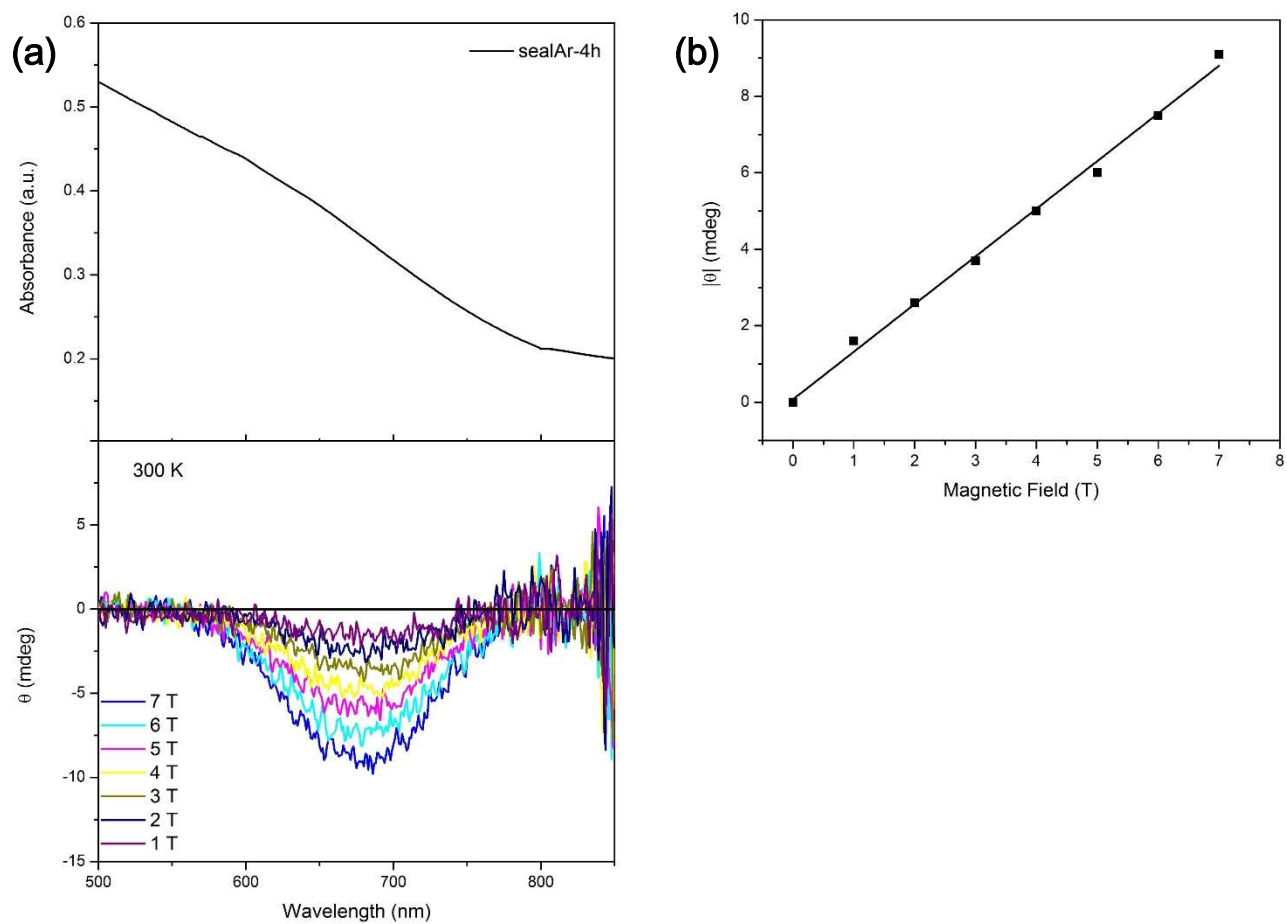
Figure 5.2 (a) Absorption and MCD spectra of sealAr-4h InN NCs collected at 300 K with various magnetic fields applied. (b) Magnetic field dependence of MCD peak intensity recorded at 685 nm for InN NCs in (a); the black line is the linear fit to the black data points.

Figure 5.2 (a) shows the bandgap absorption and the variant-field MCD spectra of sealAr-4h InN collected at 300 K. The linear field dependence of MCD signal is consistent with that in sealNH$_3$-4h, corroborating the idea that the linear field dependence of excitonic MCD signal is related to LSPR.
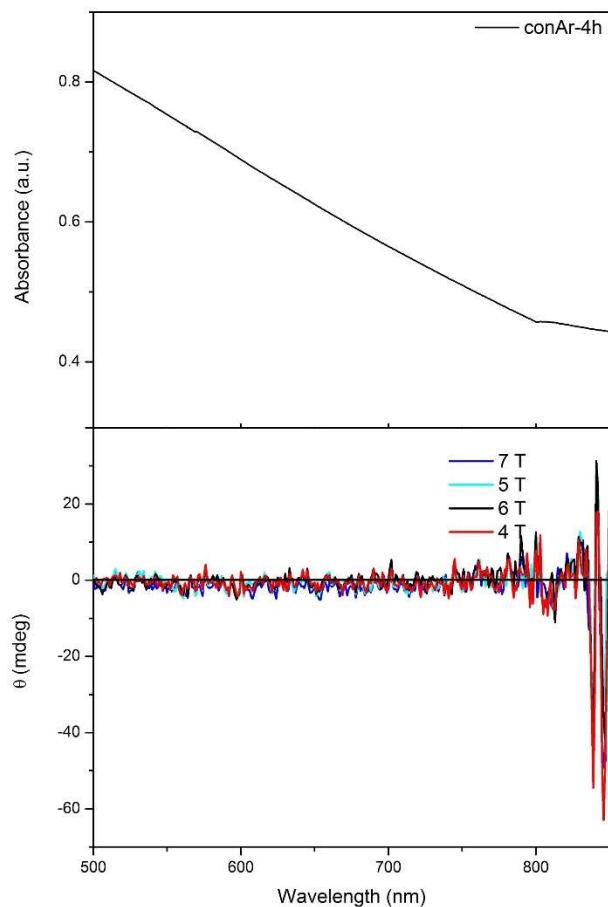
Figure 5.3 Absorption and MCD spectra of conAr-4h InN NCs collected at 300 K with various magnetic fields applied.

Moreover, the complete quench of excitonic MCD signal in the non-plasmon conAr-4h InN sample in Figure 5.3 confirms that the MCD signal originates from the LSPR. It can be seen in Figure 5.4 that the MCD maximum intensity correlates with plasmon intensity. Therefore, control of excitonic polarization can be achieved with the help of cyclotron magneto-plasmonic modes.
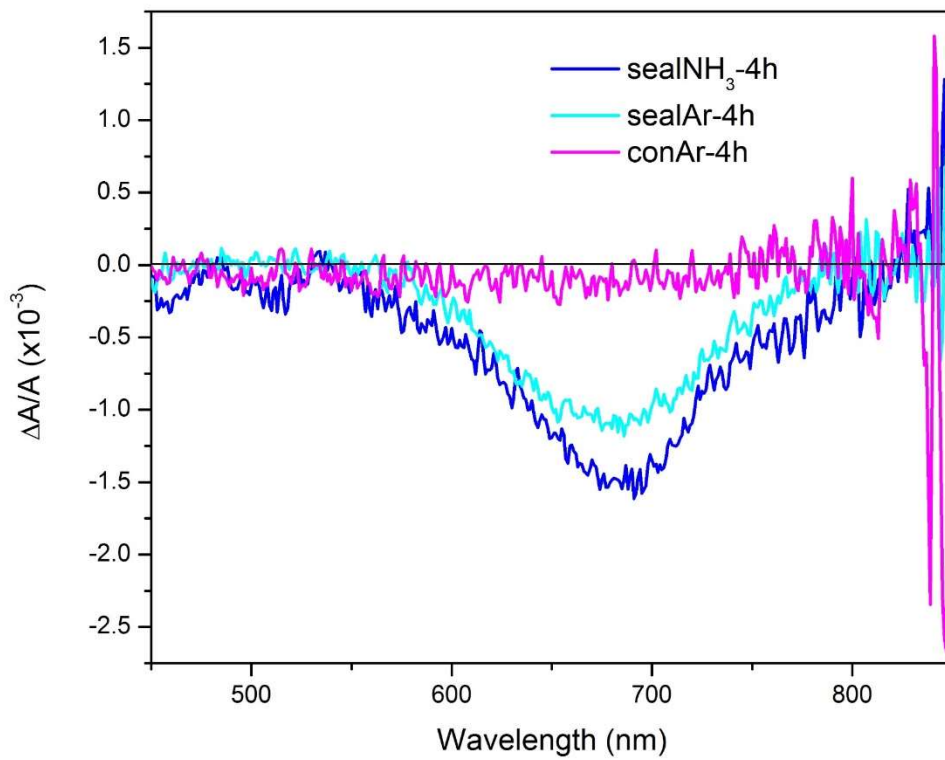
Figure 5.4 Normalized MCD spectra of sealNH$_3$-4h, sealNH$_3$-4h, and conAr-4h collected at 7 T and 300 K. The raw MCD spectra are normalized to the same absorbance at 685 nm.

In summary, the results we recorded strongly agree with what was previously reported in plasmonic transparent conducting oxides, the generality of such plasmon-controlled exciton splitting is further refined.[44,45,49] The likelihood of the appealing idea of strong plasmon-exciton coupling in semiconductor becomes additionally higher with our results. Similar to ITO and IWO,[44] the entire polarization of excitons is achieved in InN using cyclotron magnetoplasmonic modes. The preliminary hypothesis for the internal mechanism is that the polarized phonon modes help convey the angular momentum of low-energy cyclotrons to impact the chirality of the excitons, which is detailed in Section 3.2.3.[43,44] The investigation and harnessing of the plasmon–exciton interactions pave the way for technological applications in optoelectronics and quantum-information processing.

Chapter 6. Study of InN NW Growth via CVD

6.1 Structure and Morphology of InN NWs

The morphology of the as-synthesized InN NWs on the silicon substrate is obtained by SEM, and the structure is studied with the help of TEM and SAED. Figure 6.1 shows the topographic details of InN NWs synthesized at variant conditions. First of all, all chosen samples are fabricated at 480 ℃, which is the lowest temperature recorded so far using CVD. We found that any changes of temperature beyond 10 ℃ wound lead to complete sterility, so our reaction condition is in a very narrow device-specific sweet zone. A few reports discuss the positive effect of oxygen in catalyzing the formation of InN NWs via the VLS approach. From Figure 5.1 (a) to (c), the time of argon pre-purging varies, which directly affects the amount of residue oxygen in the system. It is evident in Figure 6.1 (a) that too low a percentage of oxygen would yield a large quantity of twisted NWs growing horizontally. On the contrary, as is shown in Figure 5.1 (b), abundant oxygen suppresses the growth of NWs, leaving a limited gain of straight NWs growing upwards mixed with curly wires stretching sideways. Figure 6.1 (c) demonstrate the in-between situation where both the yields and quality of straight NWs are acceptable. However, an unwanted InN carpet is layered beneath NWs under such condition. It is well reported that InN NWs grown via VLS route sprout in all directions from the gold island rather than epitaxially growing along gravity direction. The carpet could be a result of an aggregation of horizontally grown NWs. In Figure 6.1 (d), we lift the internal pressure of CVD from room pressure to 760 Torr, successfully decrease the number of by-products without sacrificing the gain. A further increase in pressure would be appreciated, while our CVD is not built for high-pressure usage and Figure 6.1 (d) is our optimal result. Besides,

EDX analysis is performed on the by-products and NWs. Due to the fact that EDX is insensitive towards nitrogen, it can only be confirmed that they both consist of only indium and nitrogen but not oxygen. The elimination of oxygen in the final product indicates that oxygen may play a part only in the early stages of NW growth.
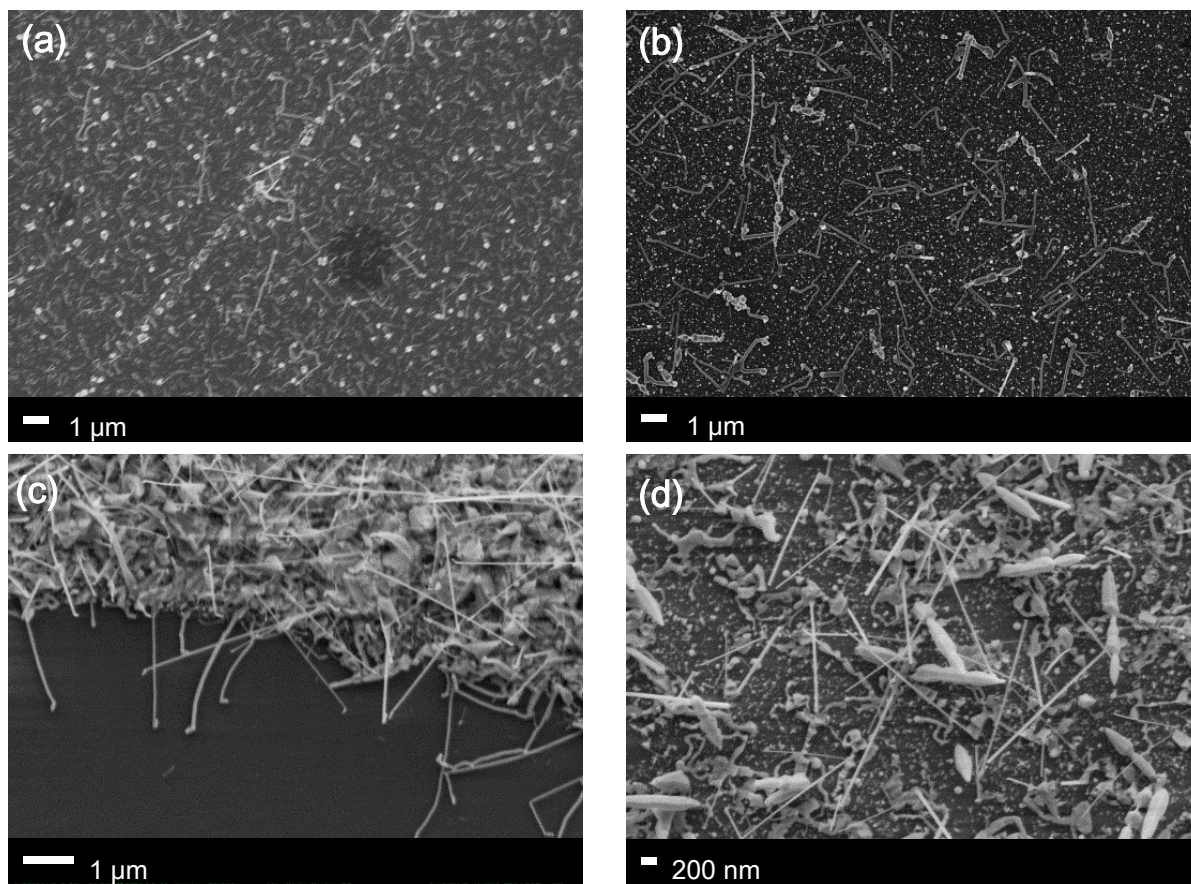
Figure 6.1 SEM graphs of InN NWs synthesized at different conditions. (a) NWs were synthesized at 480 ℃, 735 Torr. The system was pre-purged with argon for 90 min before reaction; (b) NWs were synthesized at 480 ℃, 735 Torr. The system was pre-purged with argon for 30 min before reaction; (c) NWs synthesized at 480 ℃, 735 Torr. The system is pre-purged with argon for 60

min before reaction; (d) NWs were synthesized at 480 ℃, 760 Torr. The system was pre-purged with argon for 60 min before reaction
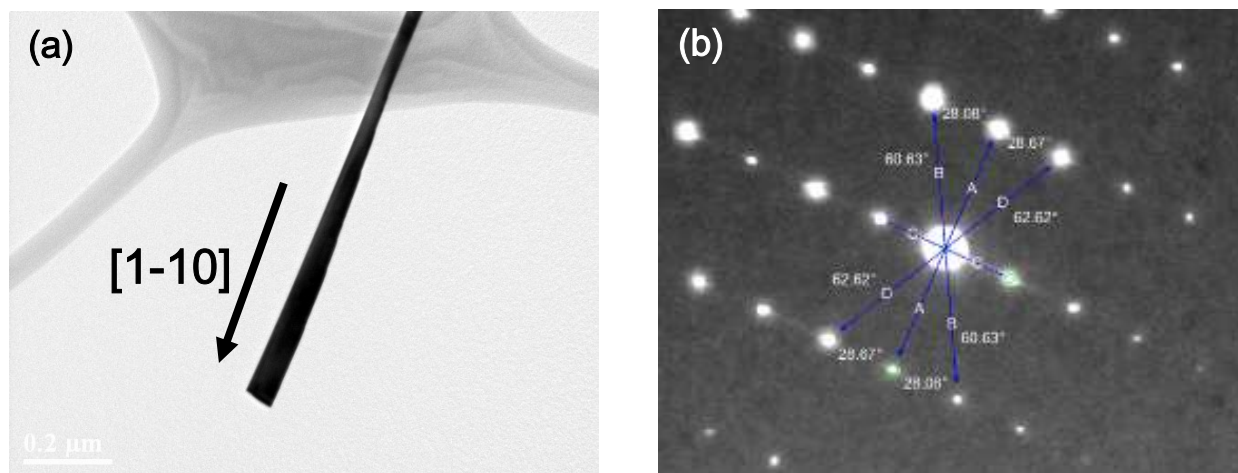
Figure 6.2 (a) TEM image of an as-synthesized InN NW in Figure 6.1 (d). (b) SAED pattern of the NW in (a).

Lattice parameter	Measured Distance (Å)	Reference Distance (Å)
a	3.53	3.533
b	3.53	3.533
c	5.69	5.693
c/a	1.61	1.61

Table 6.1 The calculated lattice parameters from Figure 1.2 (b) and the referencing lattice parameters of *wz*-InN (00-079-3498).
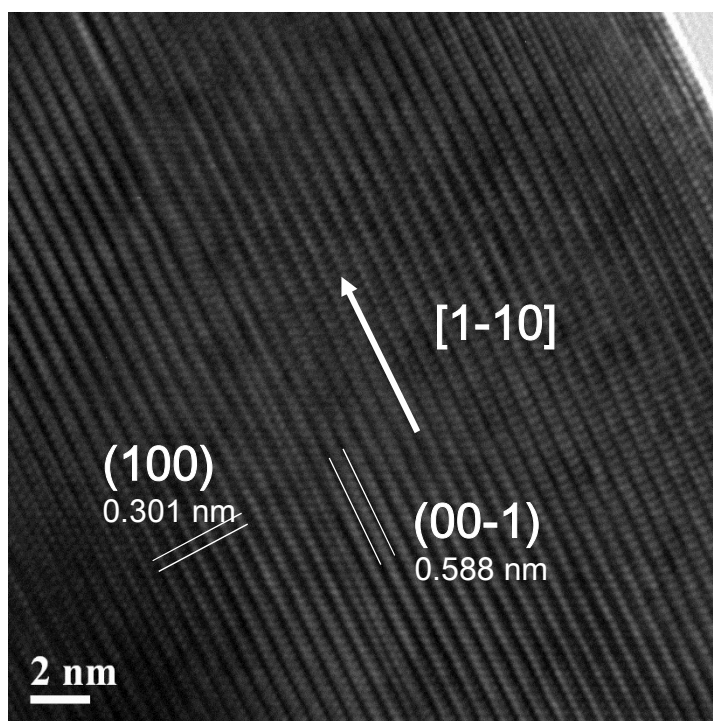
Figure 6.3 The high-resolution TEM image of one typical InN NW in Figure 6.1 (d).

The TEM image and accompanying SAED pattern in Figure 6.2 show that the straight NWs obtained are grown in the [1 -1 0] direction. By measuring the angles and comparing the calculated lattice parameters from the SAED with the reference, we confirm that *wz*-InN NWs were successfully synthesized. The average diameter of our InN NWs is about 20 nm, and the average length is above 2 μm.

Figure 6.3 suggests that the as-synthesized InN NWs are of good crystallinity. As is labeled in the figure, the lattice spacing is measured to be 3.01 Å between (1 0 0) planes of wurtzite InN and 5.88 Å between (0 0 -1) planes.

6.2 UV-Vis-NIR Absorption Spectra of InN NWs
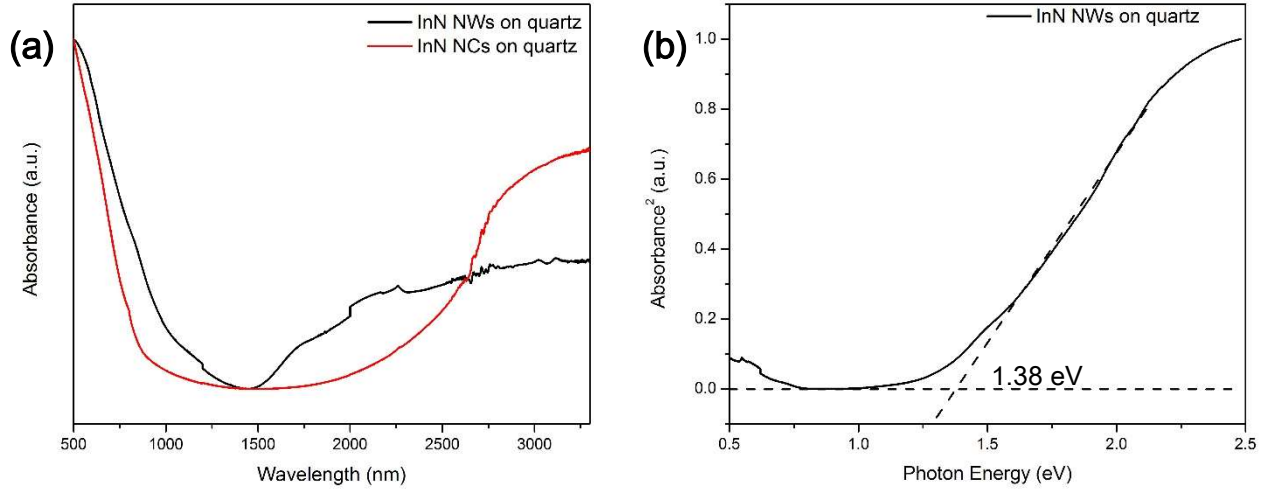
Figure 6.4 (a) The absorption of InN NWs grown on quartz and InN NCs deposited on quartz. (b) The Tauc plot of (a) to determine the bandgap of InN NWs.

From Figure 6.4, we learn that the optical properties of InN NWs and NCs are noticeably dissimilar. InN NWs have a much broader plasmon feature compared to NCs. It can be attributed to the damping from misalignments and defects in NWs, which is a common downside of low-temperature CVD synthesis. Though the intensity is low, the strength of plasmon in InN NWs is muscular at high frequency (1500-2500 nm). The apparent bandgap of InN NWs is estimated to be about 1.4 eV from Figure 6.4 (b), which indicates that it owns a lower density of free electrons than InN NCs. Since the energy distance between plasmons and excitons is shortened, enhanced exciton-plasmon coupling is expected in NWs. It can be utilized as a new platform to study the origin and applications of exciton-plasmon coupling.

In summary, *wz*-InN NWs are successfully made in the CVD machine via the VLS method. The stringent temperature, pressure, and oxygen conditions result in ultra-thin (20 nm) InN NWs with strong plasmon. The as-synthesized NWs are straight and free of oxygen contamination. Additionally, the energy gap between plasmon and exciton are reduced compared to NCs. The result satisfies our needs of exploring LSPR in the one-dimensional system and could be of great use in studying the effects of anisotropy on exciton-plasmon coupling in the future.

Chapter 7. Conclusions

This thesis demonstrates the colloidal synthesis of plasmonic pure, Al-doped, and Ti-doped InN NCs. XRD shows that *wz*-InN crystal structure is retained for both pure and doped InN NCs. The average size of the NCs increases with the synthesis time. TEM images confirm the existence of quasi-spherical InN NCs with high crystallinity.

Elemental analyses were performed on Al-doped and Ti-doped InN NCs to determine the actual doping concentration. EDX results confirm different incorporation efficiency of aluminum and titanium, and the final doping ratio is generally lower than the starting ratio. The sizes of the NCs remain mostly unchanged in all doped samples.

The UV-Vis-NIR and FTIR spectra illustrate the successful tuning of LSPR properties through varying reaction environment and adjusting doping concentration. The energy of LSPR of all as-synthesized InN NCs is unrelated to its peak absorption intensity and is around 0.37 eV (3000 cm^{-1}). Under the same reaction condition, long synthesis time results in relatively low LSPR intensity. Under the same synthesis time, by increasing the NH_3 content during the synthesis, the plasmon intensity increases, and the optical bandgap blue-shifts (1.5 - 1.75 eV). When all NH_3 gas is purged out during the reaction, plasmonic absorption quenches. For doped InN, the LSPR intensity decreases with the incorporation of aluminum. The strength surges with Ti doping at low doping concentration and plummets again with increasing doping concentration. FTIR spectra of pure and doped InN NCs indicate that plasmon intensity is in negative correlation with plasmon frequency. Raman studies suggest a relation between longitudinal-optical (LO) phonon mode and plasmon intensity.

MCD measurements provided information on the effects of LSPR properties on magneto-plasmonic modes of InN NCs. Polarized MCD spectra at the excitonic frequency of InN are obtained. The MCD signals of all measured samples are majorly temperature-independent and depend linearly on the magnetic field. The strength of MCD responses can be adjusted by tuning the InN LSPR of InN NCs, and complete quench is observed for non-plasmonic InN NCs. The above characters of our measured excitons bear strong similarities with those of cyclotrons, which attests to the idea of non-resonant plasmon-exciton coupling in semiconductors.

Finally, the synthesis of InN NWs with LSPR was demonstrated using CVD. SEM images show that the NWs have high yields and have an average diameter of around 20 nm. TEM images of as-synthesized NWs confirm good crystallinity of *wz*-InN.

In summary, LSPR-tunable *wz*-InN NCs were successfully synthesized via the colloidal method. The plasmonic properties can be controlled by changing reaction conditions and introducing Al and Ti dopants. MCD spectra of pure InN NCs have a linear dependence on the field and vary in intensity with different LSPR oscillator strengths. The intense polarization of carriers is achieved via the magneto-plasmonic coupling. The aforementioned phenomena are demonstrated for the first time in III-V semiconductor NCs and are of great significance in extending the generality of plasmon-induced exciton polarization and studying its kinetics. Moreover, plasmonic InN NWs are successfully fabricated, raising the hope of further extending the study of exciton polarization and plasmon-exciton coupling to one-dimensional semiconductor system.

The polarization of carriers via non-resonant plasmon-exciton coupling in semiconductors lays down the foundation of a new platform technology. Like spin states, the angular momentum

can be treated as new degree freedom in carriers to encode additional information. Unlike spin states, it can be optically manipulated at room temperature, which enables accessible applications. In exploring the polarization of carriers in InN NCs, this study helps facilitate the fulfillment of carrier-polarization based processors and data carriers.

Future Work

In this work, the LSPR and magneto-plasmonic properties in pure, Al-doped and Ti-doped InN NCs were studied. The influence of synthesis environment on LSPR properties of pure InN NCs is significant. EDX was performed to give the Al/In and Ti/In elemental ratio, but more measurements on In/N ratio are needed in order to study the non-stoichiometry in InN NCs. To obtain accurate In/N ratios, complete removal of nitrogen-containing surface ligands is necessary, which is challenging and requires further effort.

Our experiments on the effects of synthesis environment on plasmonic properties lack quantified expressions of NH_3 partial pressure inside the reaction chamber. A set of experiments on determining the relation between NH_3 concentrations and resulting plasmonic properties of InN are desired. Therefore, a careful experiment setup with the ability to control the reaction pressure and monitor NH_3 level would be fruitful.

The low yield and In_2S_3 contamination are significant disadvantages of our methods to synthesize Al-doped and Ti-doped InN NCs. A more diverse base of Al and Ti precursors could be explored to improve yield and doping efficiency. Better synthesizing and washing procedures are also wanted to suppress the presence of In_2S_3.

Introducing transition-metal dopants to InN NCs are also attractive future directions. The impact of magneto dipoles on plasmonic and magneto-plasmonic properties of InN NCs could be explored, which adds to the complexity and multi-functionality of our plasmonic InN NCs.

The plasmon-phonon coupling is a critical component of the hypothesis of exciton-phonon-plasmon coupling. It is crucial to figure out the correlation between phonon modes (A_1 and M_2) and plasmon-induced carrier polarization. Since A_1 and M_2 modes are IR-active, IR MCD can be applied to directly monitor their chirality under variant magnetic fields when excited at the excitonic and plasmon-resonant frequency.[80]

Finally, plasmonic InN NWs can serve as the platform for future magneto-plasmonic studies in the one-dimensional system. The effects of anisotropy on LSPR as well as electric properties would be an appealing topic. Nonetheless, devices could be built around InN NWs to study the polarization of the current induced by exciton-plasmon coupling in the NWs.

References

(1)   Afzaal, M.; O'Brien, P. Recent Developments in II-VI and III-VI Semiconductors and Their Applications in Solar Cells. *J. Mater. Chem.* **2006**, *16*, 1597–1602.

(2)   Tansley, T. L.; Egan, R. J. Defects, Optical Absorption Gallium Nitrides. *Semicond. Sci. Technol.* **1993**, *185*, 190–198.

(3)   Davydov, V. Y.; Klochikhin, A. A.; Seisyan, R. P.; Emtsev, V. V. Absorption and Emission of Hexagonal InN. *Phys. Status Solidi B* **2002**, *229*, r1–r3.

(4)   Bhuiyan, A. G.; Hashimoto, A.; Yamamoto, A. Indium Nitride (InN): A Review on Growth, Characterization, and Properties. *J. Appl. Phys.* **2003**, *94*, 2779–2808.

(5)   Wu, C.; Li, T.; Lei, L.; Hu, S.; Liu, Y.; Xie, Y. Indium Nitride from Indium Iodide at Low Temperatures: Synthesis and Their Optical Properties. *New J. Chem.* **2005**, *29*, 1610–1615.

(6)   Yamamoto, A.; Tsujino, M.; Ohkubo, M.; Hashimoto, A. Nitridation Effects of Substrate Surface on the Metalorganic Chemical Vapor Deposition Growth of InN on Si and α-Al$_2$O$_3$ Substrates. *J. Cryst. Growth* **1994**, *137*, 415–420.

(7)   Barick, B. K.; Rodríguez-Fernández, C.; Cantarero, A.; Dhar, S. Structural and Electronic Properties of InN Nanowire Network Grown by Vapor-Liquid-Solid Method. *AIP Adv.* **2015**, *5*, 057162.

(8)   Liu, Z.; Beaulac, R. Nature of the Infrared Transition of Colloidal Indium Nitride Nanocrystals: Nonparabolicity Effects on the Plasmonic Behavior of Doped Semiconductor

Nanomaterials. *Chem. Mater.* **2017**, *29*, 7507–7514.

(9)   Lee, Z. Y.; Ng, S. S.; Yam, F. K.; Hassan, Z. Influences of Elevated Thermal Decomposition of Ammonia Gas on Indium Nitride Grown by Sol–Gel Spin Coating Method. *Mater. Res. Bull.* **2017**, *96*, 258–261.

(10)   Carrier, P.; Wei, S. H. Theoretical Study of the Band-Gap Anomaly of InN. *J. Appl. Phys.* **2005**, *97*, 033707.

(11)   Mahboob, I.; Veal, T. D.; Piper, L. F. J.; McConville, C. F.; Lu, H.; Schaff, W. J.; Furthmüller, J.; Bechstedt, F. Origin of Electron Accumulation at Wurtzite InN Surfaces. *Phys. Rev. B - Condens. Matter Mater. Phys.* **2004**, *69*, 1–4.

(12)   Siddiqua, P.; O'Leary, S. K. Electron Transport within the Wurtzite and Zinc-Blende Phases of Gallium Nitride and Indium Nitride. *J. Mater. Sci. Mater. Electronics* **2018**, 29, 3511-3567.

(13)   Xiao, J.; Xie, Y.; Tang, R.; Luo, W. Benzene Thermal Conversion to Nanocrystalline Indium Nitride from Sulfide at Low Temperature. *Inorg. Chem.* **2003**, *42*, 107–111.

(14)   Hsieh, J. C.; Yun, D. S.; Hu, E.; Belcher, A. M. Ambient Pressure, Low-Temperature Synthesis and Characterization of Colloidal InN Nanocrystals. *J. Mater. Chem.* **2010**, *20*, 1435–1437.

(15)   Palomaki, P. K. B.; Miller, E. M.; Neale, N. R. Control of Plasmonic and Interband Transitions in Colloidal Indium Nitride Nanocrystals. *J. Am. Chem. Soc.* **2013**, *135*, 14142–

14150.

(16) Pitarke, J. M.; Silkin, V. M.; Chulkov, E. V.; Echenique, P. M. Theory of Surface Plasmons and Surface-Plasmon Polaritons. *Rep. prog. phys.* **2006,** 70, 1.

(17) Eustis, S.; El-Sayed, M. A. Why Gold Nanoparticles Are More Precious than Pretty Gold: Noble Metal Surface Plasmon Resonance and Its Enhancement of the Radiative and Nonradiative Properties of Nanocrystals of Different Shapes. *Chem. Soc. Rev.* **2006**, *35*, 209–217.

(18) Sherry, L. J.; Chang, S. H.; Schatz, G. C.; Van Duyne, R. P.; Wiley, B. J.; Xia, Y. Localized Surface Plasmon Resonance Spectroscopy of Single Silver Nanocubes. *Nano Lett.* **2005**, *5*, 2034–2038.

(19) Wang, F.; Shen, Y. R. General Properties of Local Plasmons in Metal Nanostructures. *Phys. Rev. Lett.* **2006**, *97*, 1–4.

(20) Willets, K. A.; Duyne, R. P. Van. Localized Surface Plasmon Resonance Spectroscopy and Sensing. *Annu. Rev. Phys. Chem.* **2007**, *58*, 267–297.

(21) Ren, M.; Chen, M.; Wu, W.; Zhang, L.; Liu, J.; Pi, B.; Zhang, X.; Li, Q.; Fan, S.; Xu, J. Linearly Polarized Light Emission from Quantum Dots with Plasmonic Nanoantenna Arrays. *Nano Lett.* **2015**, *15*, 2951–2957.

(22) Hou, W.; Cronin, S. B. A Review of Surface Plasmon Resonance-Enhanced Photocatalysis. *Adv. Funct. Mater.* **2013**, *23*, 1612–1619.

(23) Moores, A.; Goettmann, F. The Plasmon Band in Noble Metal Nanoparticles: An Introduction to Theory and Applications. *New J. Chem.* **2006**, *30*, 1121–1132.

(24) Luther, J. M.; Jain, P. K.; Ewers, T.; Alivisatos, A. P. Localized Surface Plasmon Resonances Arising from Free Carriers in Doped Quantum Dots. *Nat. Mater.* **2011**, *10*, 361–366.

(25) Lounis, S. D.; Runnerstrom, E. L.; Llordés, A.; Milliron, D. J. Defect Chemistry and Plasmon Physics of Colloidal Metal Oxide Nanocrystals. *J. Phys. Chem. Lett.* **2014**, *5*, 1564–1574.

(26) Nütz, T.; Haase, M. Wet-Chemical Synthesis of Doped Nanoparticles: Optical Properties of Oxygen-Deficient and Antimony-Doped Colloidal SnO2. *J. Phys. Chem. B* **2000**, *104*, 8430–8437.

(27) Kanehara, M.; Koike, H.; Yoshinaga, T.; Teranishi, T. Indium Tin Oxide Nanoparticles with Compositionally Tunable Surface Plasmon Resonance Frequencies in the Near-IR Region. *Jacs* **2009**, *131*, 17736–17737.

(28) Wang, T.; Radovanovic, P. V. Free Electron Concentration in Colloidal Indium Tin Oxide Nanocrystals Determined by Their Size and Structure. *J. Phys. Chem. C* **2011**, *115*, 406–413.

(29) Wu, S.; Yuan, S.; Shi, L.; Zhao, Y.; Fang, J. Preparation, Characterization and Electrical Properties of Fluorine-Doped Tin Dioxide Nanocrystals. *J. Colloid Interface Sci.* **2010**, *346*, 12–16.

(30)   Li, Y.; Cheng, J.; Liu, Y.; Liu, P.; Cao, W.; He, T.; Chen, R.; Tang, Z. Manipulation of Surface Plasmon Resonance in Sub-Stoichiometry Molybdenum Oxide Nanodots through Charge Carrier Control Technique. *J. Phys. Chem. C* **2017**, *121*, 5208–5214.

(31)   Zhao, Y.; Pan, H.; Lou, Y.; Qiu, X.; Zhu, J.; Burda, C. Plasmonic $Cu_{2-x}S$ Nanocrystals: Optical and Structural Properties of Copper-Deficient Copper(I) Sulfides. *J. Am. Chem. Soc.* **2009**, *131*, 4253–4261.

(32)   Garcia, G.; Buonsanti, R.; Runnerstrom, E. L.; Mendelsberg, R. J.; Llordes, A.; Anders, A.; Richardson, T. J.; Milliron, D. J. Dynamically Modulating the Surface Plasmon Resonance of Doped Semiconductor Nanocrystals. *Nano Lett.* **2011**, *11*, 4415–4420.

(33)   Kriegel, I.; Jiang, C.; Rodríguez-Fernández, J.; Schaller, R. D.; Talapin, D. V.; Da Como, E.; Feldmann, J. Tuning the Excitonic and Plasmonic Properties of Copper Chalcogenide Nanocrystals. *J. Am. Chem. Soc.* **2012**, *134*, 1583–1590.

(34)   Fang, H.; Hegde, M.; Yin, P.; Radovanovic, P. V. Tuning Plasmon Resonance of In_2O_3 Nanocrystals throughout the Mid-Infrared Region by Competition between Electron Activation and Trapping. *Chem. Mater.* **2017**, *29*, 4970–4979.

(35)   Mendelsberg, R. J.; Zhu, Y.; Anders, A. Determining the Nonparabolicity Factor of the CdO Conduction Band Using Indium Doping and the Drude Theory. *J. Phys. D. Appl. Phys.* **2012**, *45,* 425302.

(36)   Hasselbeck, M. P.; Enders, P. M. Electron-Electron Interactions in the Nonparabolic Conduction Band of Narrow-Gap Semiconductors. *Phys. Rev. B - Condens. Matter Mater.*

Phys. **1998**, *57*, 9674–9681.

(37) Ghosh, S. K.; Nath, S.; Kundu, S.; Esumi, K.; Pal, T. Solvent and Ligand Effects on the Localized Surface Plasmon Resonance (LSPR) of Gold Colloids. *J. Phys. Chem. B* **2004**, *108*, 13963–13971.

(38) Cao, E.; Lin, W.; Sun, M.; Liang, W.; Song, Y. Exciton-Plasmon Coupling Interactions: From Principle to Applications. *Nanophotonics* **2018**, *7*, 145–167.

(39) Okamoto, K.; Niki, I.; Shvartser, A.; Narukawa, Y.; Mukai, T.; Scherer, A. Surface-Plasmon-Enhanced Light Emitters Based on InGaN Quantum Wells. *Nat. Mater.* **2004**, *3*, 601–605.

(40) Okamoto, K.; Funato, M.; Kawakami, Y.; Tamada, K. High-Efficiency Light Emission by Means of Exciton – Surface-Plasmon Coupling. *J. Photochem. Photobiol. C. Rev.* **2017**, *32*, 58–77.

(41) Uchida, K.; Adachi, H.; Kikuchi, D.; Ito, S.; Qiu, Z.; Maekawa, S.; Saitoh, E. Generation of Spin Currents by Surface Plasmon Resonance. *Nat. Commun.* **2015**, *6*, 1–8.

(42) Zhang, J.; Tang, Y.; Lee, K.; Ouyang, M. Tailoring Light-Matter-Spin Interactions in Colloidal Hetero-Nanostructures. *Nature* **2010**, *466*, 91–95.

(43) Fert, A. Origin, Development, and Future of Spintronics (Nobel Lecture). *Angew. Chemie - Int. Ed.* **2008**, *47*, 5956–5967.

(44) Yin, P.; Tan, Y.; Fang, H.; Hegde, M.; Radovanovic, P. V. Plasmon-Induced Carrier

Polarization in Semiconductor Nanocrystals. *Nat. Nanotechnol.* **2018**, *13*, 463–467.

(45)   Yin, P.; Hegde, M.; Tan, Y.; Chen, S.; Garnet, N.; Radovanovic, P. V. Controlling the Mechanism of Excitonic Splitting in In_2O_3 Nanocrystals by Carrier Delocalization. *ACS Nano* **2018**, *12*, 11211–11218.

(46)   Solomon, E. I.; Pavel, E. G.; Loeb, K. E.; Campochiaro, C. Magnetic Circular Dichroism Spectroscopy as a Probe of the Geometric and Electronic Structure of Non-Heme Ferrous Enzymes. *Coord. Chem. Rev.* **1995**, *144*, 369–460.

(47)   Pineider, F.; Campo, G.; Bonanni, V.; Fernández, C. D. J.; Mattei, G.; Caneschi, A.; Gatteschi, D.; Sangregorio, C. Circular Magnetoplasmonic Modes in Gold Nanoparticles. *Nano Lett.* **2013**, *13*, 4785–4789.

(48)   Hartstein, K. H.; Schimpf, A. M.; Salvador, M.; Gamelin, D. R. Cyclotron Splittings in the Plasmon Resonances of Electronically Doped Semiconductor Nanocrystals Probed by Magnetic Circular Dichroism Spectroscopy. *J. Phys. Chem. Lett.* **2017**, *8*, 1831–1836.

(49)   Yin, P.; Hegde, M.; Garnet, N. S.; Tan, Y.; Radovanovic, P. V. Faceting-Controlled Zeeman Splitting in Plasmonic TiO_2 Nanocrystals. *Nano Lett.* **2019**, *19*, 6695–6702.

(50)   Jung, W. S.; Choon, S. R.; Mini, B. K. Growth of Nano- and Microstructured Indium Nitride Crystals by the Reaction of Indium Oxide with Ammonia. *Bull. Korean Chem. Soc.* **2005**, *26*, 1354–1358.

(51)   Demangeot, F.; Frandon, J.; Pinquier, C.; Caumont, M.; Briot, O.; Maleyre, B.; Clur-

Ruffenach, S.; Gil, B. InN Nanostructures: Strain and Morphology. *Mater. Res. Soc. Symp. - Proc.* **2003**, *798*, 175–180.

(52)   Hsu, S.-W.; Bryks, W.; Tao, A. R. Effects of Carrier Density and Shape on the Localized Surface Plasmon Resonances of $Cu_{2-x}S$ Nanodisks. *Chem. Mater.* **2012**, *24*, 3765–3771.

(53)   Wei, T.; Liu, Y.; Dong, W.; Zhang, Y.; Huang, C.; Sun, Y.; Chen, X.; Dai, N. Surface-Dependent Localized Surface Plasmon Resonances in CuS Nanodisks. *ACS Appl. Mater. Interfaces* **2013**, *5*, 10473–10477.

(54)   Hsu, S.-W.; On, K.; Tao, A. R. Localized Surface Plasmon Resonances of Anisotropic Semiconductor Nanocrystals. *J. Am. Chem. Soc.* **2011**, *133*, 19072–19075.

(55)   Wu, C. Y.; Pan, Z. Q.; Liu, Z.; Wang, Y. Y.; Liang, F. X.; Yu, Y. Q.; Wang, L.; Luo, L. B. Controllable Synthesis of P-Type Cu_2S Nanowires for Self-Driven NIR Photodetector Application. *J. Nanoparticle Res.* **2017**, *19*, 1–9.

(56)   Hegde, M.; Farvid, S. S.; Hosein, I. D.; Radovanovic, P. V. Tuning Manganese Dopant Spin Interactions in Single GaN Nanowires at Room Temperature. *ACS Nano* **2011**, *5*, 6365–6373.

(57)   Farvid, S. S.; Hegde, M.; Hosein, I. D.; Radovanovic, P. V. Electronic Structure and Magnetism of Mn Dopants in GaN Nanowires: Ensemble vs Single Nanowire Measurements. *Appl. Phys. Lett.* **2011**, *99*, 97–100.

(58)   Hegde, M.; Hosein, I. D.; Sabergharesou, T.; Farvid, S. S.; Radovanovic, P. V. Introducing

and Manipulating Magnetic Dopant Exchange Interactions in Semiconductor Nanowires. *Proc. SPIE* **2013**, *8813*, 88132S.

(59)   Jie, J.; Zhang, W.; Bello, I.; Lee, C. S.; Lee, S. T. One-Dimensional II-VI Nanostructures: Synthesis, Properties and Optoelectronic Applications. *Nano Today* **2010**, *5*, 313–336.

(60)   Chang, D. E.; Sørensen, A. S.; Hemmer, P. R.; Lukin, M. D. Quantum Optics with Surface Plasmons. *Phys. Rev. Lett.* **2006**, *97*, 1–4.

(61)   Pyayt, A. L.; Wiley, B.; Xia, Y.; Chen, A.; Dalton, L. Integration of Photonic and Silver Nanowire Plasmonic Waveguides. *Nat. Nanotechnol.* **2008**, *3*, 660–665.

(62)   Tian, Y.; Bakaul, S. R.; Wu, T. Oxide Nanowires for Spintronics: Materials and Devices. *Nanoscale* **2012**, *4*, 1529–1540.

(63)   Amendola, V.; Pilot, R.; Frasconi, M.; Maragò, O. M.; Iatì, M. A. Surface Plasmon Resonance in Gold Nanoparticles: A Review. *J. Phys. Condens. Matter* **2017**, *29*, 203002.

(64)   Lan, Z. H.; Wang, W. M.; Sun, C. L.; Shi, S. C.; Hsu, C. W.; Chen, T. T.; Chen, K. H.; Chen, C. C.; Chen, Y. F.; Chen, L. C. Growth Mechanism, Structure and IR Photoluminescence Studies of Indium Nitride Nanorods. *J. Cryst. Growth* **2004**, *269*, 87–94.

(65)   Papageorgiou, P.; Zervos, M.; Othonos, A. An Investigation into the Conversion of In_2O_3 into InN Nanowires. *Nanoscale Res. Lett.* **2011**, *6*, 3–7.

(66)   Tang, T.; Han, S.; Jin, W.; Liu, X.; Li, C.; Zhang, D.; Zhou, C.; Chen, B.; Han, J.; Meyyapan,

M. Synthesis and Characterization of Single-Crystal Indium Nitride Nanowires. *J. Mater. Res.* **2004**, *19*, 423–426.

(67) Radovanovic, P. V; Barrelet, C. J.; Gradec, S.; Lieber, C. M. General Synthesis of Manganese-Doped II − VI and III − V Semiconductor Nanowires. *Nano* **2005**, *5*, 1407-1411.

(68) Liang, C. H.; Chen, L. C.; Hwang, J. S.; Chen, K. H.; Hung, Y. T.; Chen, Y. F. Selective-Area Growth of Indium Nitride Nanowires on Gold-Patterned Si(100) Substrates. *Appl. Phys. Lett.* **2002**, *81*, 22–24.

(69) Wang, Y.; Hegde, M.; Chen, S.; Yin, P.; Radovanovic, P. V. Control of the Spontaneous Formation of Oxide Overlayers on GaP Nanowires Grown by Physical Vapor Deposition. *AIMS Mater. Sci.* **2018**, *5*, 105–115.

(70) Law, M.; Goldberger, J.; Yang, P. Semiconductor Nanowires and Nanotubes. *Annu. Rev. Mater. Res.* **2004**, *34*, 83–122.

(71) Yang, P.; Yan, R.; Fardy, M. Semiconductor Nanowire: Whats Next? *Nano Lett.* **2010**, *10*, 1529–1536.

(72) Morales, A.M and Lieber, C. M. A Laser Ablation Method for the Synthesis of Crystalline Semiconductor Nanowires. *Science* **1998**, *279*, 208–211.

(73) Kao, M.; Erasmus, R. M.; Moloto, N.; Coville, N. J.; Mhlanga, S. D. UV-Assisted Synthesis of Indium Nitride Nano and Microstructures. *J. Mater. Chem. A* **2015**, *3*, 5962–5970.

(74) Liu, Z.; Janes, L. M.; Saniepay, M.; Beaulac, R. Charge Storage and Quantum Confinement

Resilience in Colloidal Indium Nitride Nanocrystals. *Chem. Mater.* **2018**, *30*, 5435–5443.

(75) Zandi, O.; Agrawal, A.; Shearer, A. B.; Reimnitz, L. C.; Dahlman, C. J.; Staller, C. M.; Milliron, D. J. Impacts of Surface Depletion on the Plasmonic Properties of Doped Semiconductor Nanocrystals. *Nat. Mater.* **2018**, *17*, 710–717.

(76) Roth, A. P.; Webb, J. B.; Williams, D. F. Band-Gap Narrowing in Heavily Defect-Doped ZnO. *Phys. Rev. B* **1982**, *25*, 7836–7839.

(77) Alarcón-Lladó, E.; Brazzini, T.; Ager, J. W. Surface Origin and Control of Resonance Raman Scattering and Surface Band Gap in Indium Nitride. *J. Phys. D. Appl. Phys.* **2016**, *49*, 255102.

(78) Askari, S.; Mariotti, D.; Stehr, J. E.; Benedikt, J.; Keraudy, J.; Helmersson, U. Low-Loss and Tunable Localized Mid-Infrared Plasmons in Nanocrystals of Highly Degenerate InN. *Nano Lett.* **2018**, *18*, 5681–5687.

(79) Domènech-Amador, N.; Cuscó, R.; Artús, L.; Yamaguchi, T.; Nanishi, Y. Raman Scattering Study of Anharmonic Phonon Decay in InN. *Phys. Rev. B - Condens. Matter Mater. Phys.* **2011**, *83*, 1–12.

(80) Davydov, V. Y.; Klochikhin, A. A.; Smirnov, A. N.; Strashkova, I. Y.; Krylov, A. S.; Lu, H.; Gwo, S. Selective excitation of E_1 (LO) and A_1 (LO) phonons with large wave vectors in the Raman spectra of hexagonal InN. *Phys. Rev. B* **2009**, *80*, 081204.

(81) Chen, S.Y.; Zheng, C.; Fuhrer, M.S.; Yan, J. Helicity-resolved Raman scattering of MoS_2,

MoSe$_2$, WS$_2$, and WSe$_2$ atomic layers. *Nano lett*. **2015**, *15*, 2526–2532.

(82) Zhu, H.; Yi, J.; Li, M.Y.; Xiao, J.; Zhang, L.; Yang, C.W. Kaindl, R.A., Li, L.J., Wang, Y.; Zhang, X. Observation of chiral phonons. *Science* **2018**, *359*, 579–582.

(83) Liu, H.; Dou, Q.; Chua, C.S. Integration of p-type β-In$_2$S$_3$ thin films on III-nitride heterostructures for multiple functional applications. *RSC Adv.* **2016**, *6*, 94139–94148.

(84) Schäfer-Nolte, E.O.; Stoica, T.; Gotschke, T.; Limbach, F.A.; Sutter, E.; Sutter, P.; Grützmacher, D.; Calarco, R. Enhanced light scattering of the forbidden longitudinal optical phonon mode studied by micro-Raman spectroscopy on single InN nanowires. *Nanotechnology* **2010**, *21*, 315702.
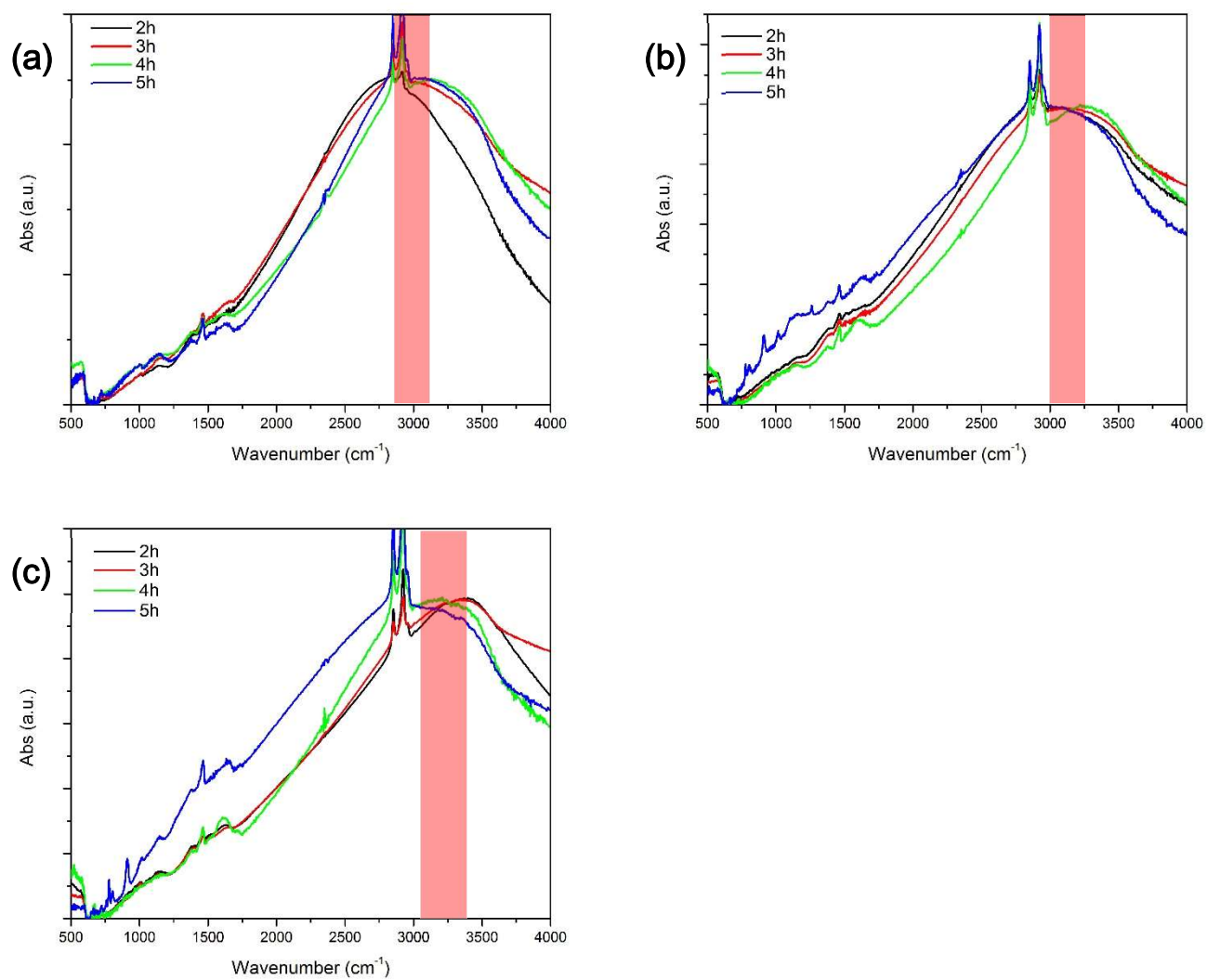
Appendix

Figure A1. Normalized LSPR absorption spectra of InN NCs in the IR range. The graphs are arranged by the reaction condition: (a) sealNH$_3$, (b) sealAr, and (c) conNH$_3$.
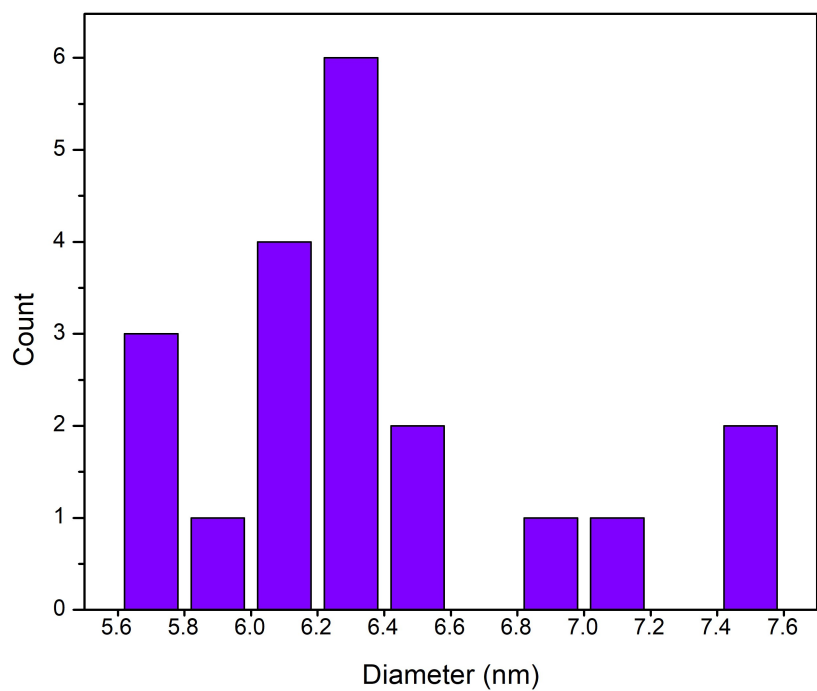
Figure A2. The size distribution diagram of 30%Al-doped InN NCs in Figure 4.2 (b). Twenty

NCs were randomly chosen, and their diameters were measured to create the diagram.

Starting Al concentration (%)	Actual Al concentration (%)	Relative LSPR Intensity (a.u.)	Starting Ti concentration (%)	Actual Ti concentration (%)	Relative LSPR Intensity (a.u.)
10	6.5	0.56	5	1.8	1.03
20	9.9	0.54	10	2.1	1.21
30	15.2	0.36	15	4.8	0.68
40	20.6	0.31	20	6.5	0.43

Table A1. Comparison of actual doping concentration and relative LSPR intensity of Al-doped and Ti-doped InN NCs. The relative LSPR intensities are determined assuming that pure InN has a relative LSPR intensity of 1.